# Distinct mechanisms underlie the subsynaptic mobility of presynaptic metabotropic glutamate receptor types to tune receptor activation

Anna Bodzęta[1], Florian Berger[1], and Harold D. MacGillavry[1,*]

[1] Division of Cell Biology, Neurobiology and Biophysics, Department of Biology, Faculty of Science, Utrecht University, 3584 CH, The Netherlands.

[*]Correspondence: h.d.macgillavry@uu.nl (HDM)

## ABSTRACT

Presynaptic metabotropic glutamate receptors (mGluRs) are essential for activity-dependent modulation of synaptic transmission in the brain. However, the mechanisms that control the subsynaptic distribution and mobility of these receptors to contribute to their function are poorly understood. Here, using super-resolution microscopy and single-molecule tracking, we provide novel insights in the molecular mechanisms that control the spatial distribution and mobility of presynaptic mGluRs. We demonstrate that mGluR2 localizes diffusely along the axon and boutons and is highly mobile, while mGluR7 is immobilized specifically at the active zone, indicating that distinct mechanisms underlie the dynamic distribution of these receptor types. Indeed, we found that the positioning of mGluR2 is modulated by intracellular interactions. In contrast, immobilization of mGluR7 at the active zone is mediated by its extracellular domain that interacts in *trans* with the postsynaptic adhesion molecule ELFN2. Moreover, we found that receptor activation or changing synaptic activity does not alter the surface mobility of presynaptic mGluRs. Additionally, computational modeling of presynaptic mGluRs activity revealed that the precise subsynaptic localization of mGluRs determines their activation probability and thus directly impacts their ability to modulate neurotransmitter release. Altogether, this study demonstrates that distinct mechanisms control surface mobility of presynaptic mGluRs to differentially contribute to the regulation of glutamatergic synaptic transmission.

## INTRODUCTION

Activity-directed modulation of synaptic efficacy underlies the ability of neuronal networks to process and store information. Presynaptic mechanisms that impinge on the neurotransmitter release machinery are a critical factor in fine tuning synaptic efficacy. In particular, presynaptic metabotropic glutamate receptors (mGluRs) are essential negative-feedback control elements that modulate transmission by dampening glutamate release (Pinheiro and Mulle, 2008; Reiner and Levitz, 2018). Disruptions in these receptor systems severely deregulate synaptic function and specific forms of synaptic plasticity, and aberrant mGluR function has been associated with several neurological disorders such as anxiety, epilepsy and schizophrenia, further highlighting their physiological importance (Muly et al., 2007; Sansig et al., 2001; Woolley et al., 2008). Nevertheless, it remains poorly understood how these receptors are organized at presynaptic sites to efficiently modulate transmission.

The eight known mGluRs (mGluR1 – mGluR8) belong to the class C G-protein-coupled receptors (GPCRs). These GPCRs exist as constitutive dimers and have a distinctive large extracellular domains (ECD) that contains the ligand-binding domain connected to the prototypical 7-helix transmembrane domain (TMD) via a cysteine-rich domain. mGluRs are further divided into three groups based on their sequence homology, downstream signaling partners and agonist selectivity (Niswender and Conn, 2010). These functionally diverse groups are expressed throughout the central nervous system but are generally targeted to specific subcellular locations. Group I mGluRs (mGluR1/5) are primarily expressed at postsynaptic sites, group II mGluRs (mGluR2/3) are present at both pre- and postsynaptic sites, and group III mGluRs (mGluR4, mGluR6-8) are located almost exclusively at presynaptic sites (Petralia et al., 1996; Shigemoto et al., 1996). The presynaptic group II and III mGluRs mGluR2 and mGluR7 are both abundantly expressed in the hippocampus (Kinoshita et al., 1998), share substantial homology (~60%), and both couple to inhibitory G-proteins ($G\alpha_{i/o}$) that repress adenylyl cyclase activity. Nevertheless, these receptors differ significantly in their pharmacological characteristics and interactome, conferring functionally distinct roles to these receptors in synaptic transmission and plasticity.

Generally, activation of presynaptic mGluRs depresses synaptic transmission via inhibition of voltage-gated $Ca^{2+}$-channels (VGCC), activation of $K^{+}$ channels, or by directly modulating components of the release machinery such as Munc13, Munc18 and RIM-1 (de Jong and Verhage, 2009; Pinheiro and Mulle, 2008). As such, these receptors have been implicated in the regulation of both short-term plasticity as well as long-term depression of synaptic responses (Kamiya and Ozawa, 1999; Martín et al., 2007; Millán et al., 2002; Okamoto et al., 1994; Pelkey et al., 2008, 2005; Robbe et al., 2002). However, signaling events downstream of presynaptic mGluRs can also potentiate release, and particularly mGluR7 has been postulated to bidirectionally regulate synaptic transmission (Dasgupta et al., 2020; Klar et al., 2015; Martín et al., 2018, 2010). Thus, presynaptic mGluRs modulate synaptic transmission through a variety of downstream effectors, and the functional outcome of mGluR activation is probably determined by the frequency and duration of synaptic signals. Additionally, the subsynaptic distribution and dynamics of presynaptic mGluRs are likely to influence their ability to become activated and engage local downstream signaling partners. In particular, since these receptors have different affinities for glutamate, their subsynaptic position relative to the point of glutamate release ultimately determines their probability of activation. mGluR2 has a moderate to high affinity for glutamate (in the micromolar range) and its positioning relative to the release site might thus only modestly affect its contribution to regulating release probability. In contrast, when measured in non-neuronal cells, the affinity of mGluR7 for glutamate is exceptionally low, in the millimolar range (0.5-2.5 mM) (Schoepp et al., 1999). In addition, mGluRs are obligatory dimers and activation of single subunits in an mGluR dimer produces only low-efficacy activation. Given that release events produce only brief, 1-3 mM peaks in glutamate concentration in the synaptic cleft (Diamond and Jahr, 1997; Lisman et al., 2007), it has thus been questioned whether mGluR7 at neuronal synapses, even when placed immediately adjacent to release sites, will ever be exposed to sufficient levels of glutamate to become activated. However, this is in contrast with the wealth of physiological evidence from different model systems that show that mGluR7 is a key modulator of synaptic transmission (Bushell et al., 2002; Klar et al., 2015; Martín et al., 2018; Millán et al., 2002; Pelkey et al., 2008, 2005; Sansig et al., 2001). Interestingly, recent evidence indicated that the postsynaptic adhesion proteins ELFN1 and 2 (extracellular leucine-rich repeat and fibronectin type III domain-containing 1 and 2) transsynaptically interact with mGluR7 to confer allosteric modulation of the receptor, potentially altering the threshold for mGluR7 activation within the context of individual synapses (Dunn et al., 2019b; Stachniak et al., 2019; Sylwestrak and Ghosh, 2012; Tomioka et al., 2014). Thus, the precise localization of presynaptic mGluRs determines their activation probability and greatly impacts their ability to modulate synaptic transmission through local downstream effectors. Nevertheless, quantitative insight in the dynamic distribution of presynaptic mGluRs in live neurons and the mechanisms that control their dynamic positioning is lacking.

Here, to understand how mGluR2 and mGluR7 contribute to synaptic transmission, we studied how the dynamic positioning of subsynaptic distribution of these receptors is mechanistically controlled. Using complementary super-resolution imaging approaches, we found that mGluR2 is highly dynamic and localized throughout the axon, while mGluR7 is immobilized at presynaptic active zones. Surprisingly, we found that the specific positioning of mGluR7 is not controlled by intracellular interactions but relies on extracellular interactions. Specifically, we identified that the ECD of mGluR7, that interacts with the postsynaptic protein ELFN2, is required for anchoring mGluR7 at the active zone.

Furthermore, a computational model of mGluR activation at presynaptic sites indicates that mGluR2 activation is only loosely coupled to release site location, while activation of mGluR7 is inefficient, even when localized within a few nanometers of the release site or during high-frequency stimulation patterns. Based on our findings, we propose that the different mechanisms that control presynaptic mGluR positioning ensure the differential contribution of these receptors to transmission.

## RESULTS

### Distinct differences in the subsynaptic distribution of presynaptic mGluR subtypes

The precise spatial distribution of mGluR subtypes at presynaptic sites likely determines their functional contribution to the modulation of synaptic transmission. To compare the subsynaptic distribution of presynaptic group II and III mGluRs in hippocampal neurons, we determined the localization of mGluR2 (group II) and mGluR7 (group III) relative to the active zone marker Bassoon (Bsn) using two-color gated stimulated emission depletion (gSTED) super-resolution microscopy. To visualize mGluR2, we tagged endogenous mGluR2 with super-ecliptic pHluorin (SEP), a pH-sensitive variant of GFP, using a recently developed CRISPR/Cas9-mediated knock-in approach (Willems et al., 2020). Because the level of endogenous mGluR2 expression was low, we enhanced the SEP signal using anti-GFP staining to reliably measure mGluR2 distribution. We found that mGluR2 was localized both in axons and dendrites (Figure 1 - figure supplement 1A), as reported previously (Ohishi et al., 1994), but even though an earlier study suggested that mGluR2 is located in the preterminal region of the axon, and not in presynaptic boutons (Shigemoto et al., 1997), we detected mGluR2 both in the axon shaft and within synaptic boutons (Figure 1A). However, as is apparent from line profiles of the fluorescence intensity of mGluR2 signal along Bsn-labeled puncta, the mGluR2 signal was largely excluded from presynaptic active zones (Figure 1B). Confirming this finding, a similar distribution pattern was observed using antibody labeling for mGluR2/3 (Figure 1 - figure supplement 1B, C), further indicating that presynaptic group II mGluRs are distributed throughout the axon but excluded from active zones. Immunostaining for the group III mGluR, mGluR7 labeled a subset of neurons in our cultures (Figure 1C and Figure 1 - figure supplement 1D), consistent with previous studies (Shigemoto et al., 1996; Tomioka et al., 2014). In contrast to mGluR2, line profiles indicated that the maximum intensity of mGluR7 labeling coincided with the Bsn-marked active zone (Figure 1D). Co-localization analysis further confirmed this, showing that the majority of mGluR7-positive puncta overlap with Bsn-positive puncta, while mGluR2 labeling showed a striking lack of overlap with Bsn (co-localization with Bsn-positive puncta, mGluR2: 0.12 ± 0.02, mGluR7: 0.54 ± 0.03; Figure 1E). Together, these results indicate that two presynaptic mGluR subtypes that are both implicated in the regulation of presynaptic release properties, have distinct subsynaptic distribution patterns.

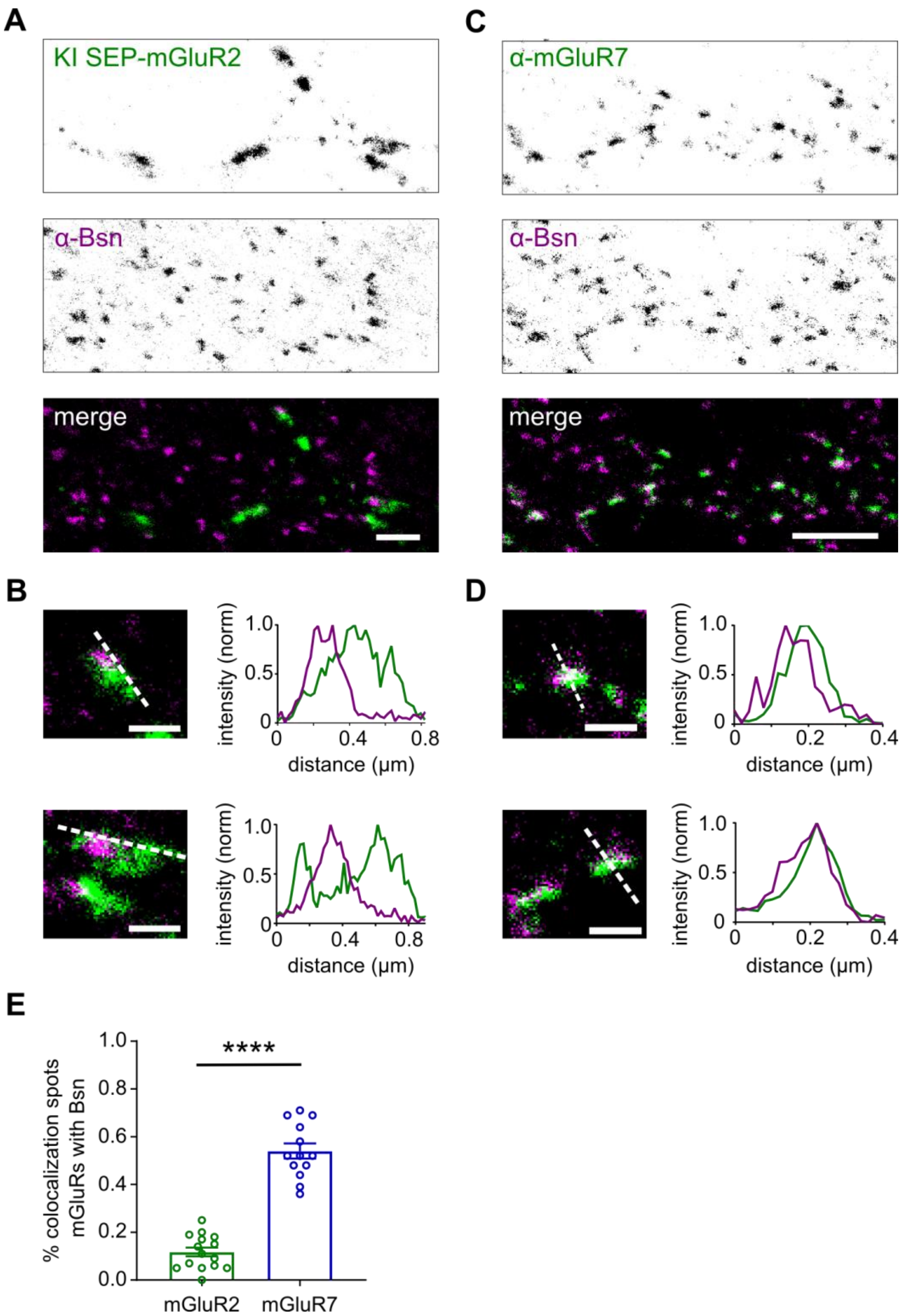


**Figure 1:** Subsynaptic distribution of presynaptic mGluRs. **(A)** gSTED image of SEP-mGluR2 CRISPR/Cas9 knock-in neuron co-stained with anti-Bassoon (STAR635P) (Bsn). Note that due to the low endogenous expression level of mGluR2, SEP signal was enhanced with anti-GFP (STAR580) staining. Scale bar, 2 µm. **(B)** Example images and intensity profiles of individual mGluR2 positive synapses from **(A)**. Scale bar, 500 nm. **(C)** gSTED image of neuron co-stained with anti-mGluR7 (STAR580) and anti-Bsn (STAR635P). Scale bar, 2 µm. **(D)** Example images and intensity profiles of individual mGluR7-positive synapses from **(C)**. Scale bar: 500 nm. **(E)** Quantification of co-localization between presynaptic mGluRs and Bsn. Unpaired *t*-test, *** $P < 0.001$.

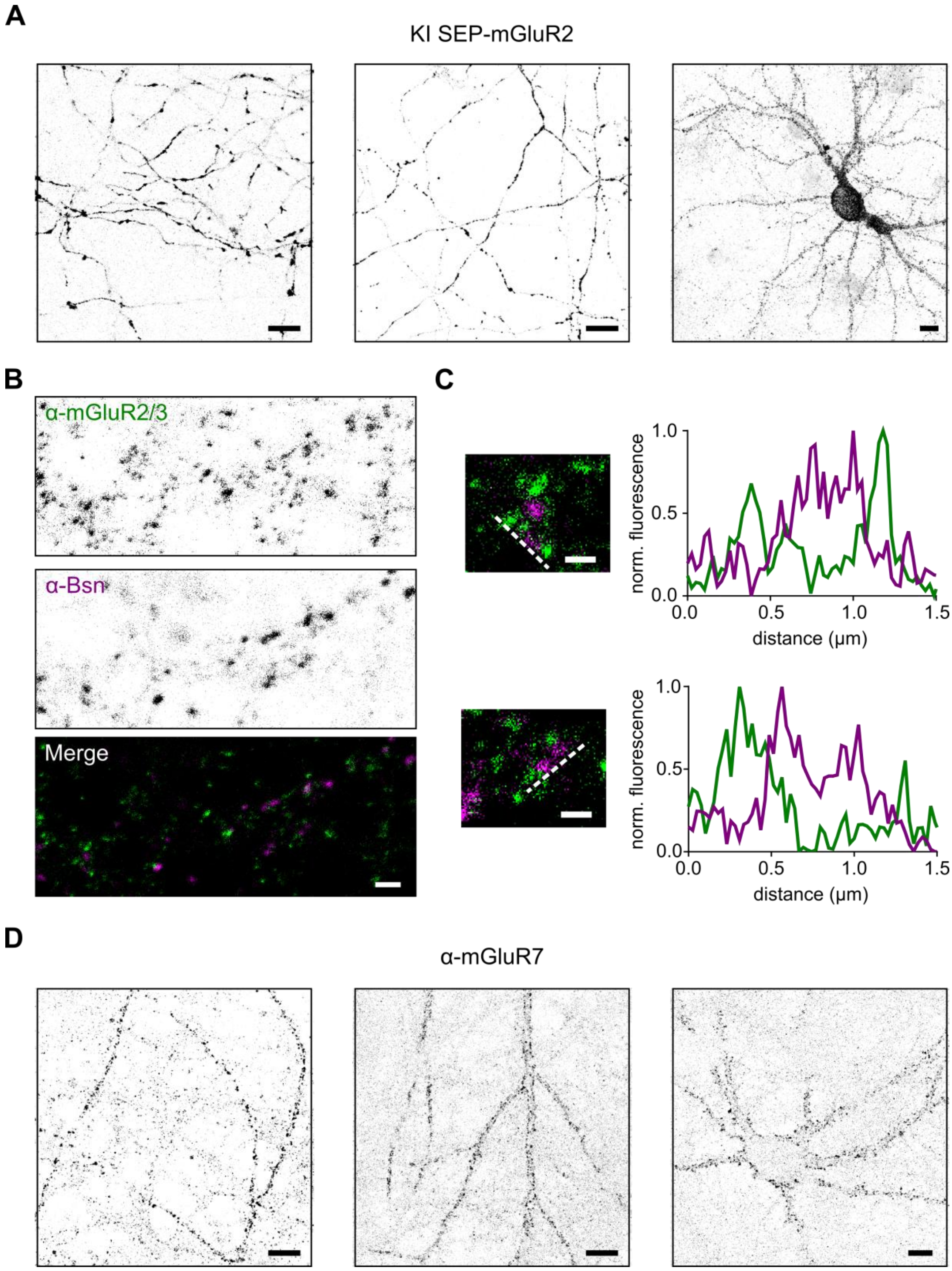


**Figure supplement 1.** Distribution of presynaptic mGluRs. **(A)** Example confocal images of SEP-mGluR2 knock-in neurons. SEP signal was enhanced with anti-GFP (STAR580) staining. Scale bar 10 μm. **(B)** gSTED image of neuron co-stained with anti-mGluR2/3 (STAR580) and anti-Bassoon (STAR635P) (Bsn). Scale bar, 2 μm. **(C)** Example images and intensity profiles of individual mGluR2/3 positive synapses from **(B)**. Scale bar, 500 nm. **(D)** Example confocal images of neurons stained with anti-mGluR7 (STAR580). Scale bar, 10 μm.

**Differential stability of mGluR2 and mGluR7 at presynaptic boutons**

To test if the observed receptor distributions reflect differences in surface mobility in the axonal membrane, we expressed SEP-tagged mGluR2 and mGluR7 to visualize surface-expressed receptors in live cells and performed fluorescence recovery after photobleaching (FRAP) experiments. Importantly, we found that expressed receptors were efficiently targeted to axons and their localization was consistent with the observed endogenous distributions. SEP-mGluR7 was enriched in presynaptic boutons, while SEP-mGluR2 expression was more diffuse throughout the axon (Figure 2- figure supplement 2). We photobleached the fluorescence in small regions overlapping with presynaptic boutons and monitored the recovery of fluorescence over time. Strikingly, the recovery of fluorescence was much more rapid and pronounced for SEP-mGluR2 than for SEP-mGluR7 (Figure 2A, B). Indeed, quantification of the fluorescence recovery curves showed that the mobile fraction (SEP-mGluR2: 0.60 ± 0.04, SEP-mGluR7: 0.29 ± 0.03, $P<0.0005$, unpaired *t*-test; Figure 2D) and the recovery half-time (SEP-mGluR2 15.0 ± 1.8 s, SEP-mGluR7 23.5 ± 2.3 s, $P<0.05$, unpaired *t*-test; Figure 2C) of SEP-mGluR2 were significantly higher than observed for SEP-mGluR7. Thus, these results indicate that mGluR2 is highly mobile in axons, while mGluR7 is immobilized at presynaptic sites and displays minor exchange between synapses.

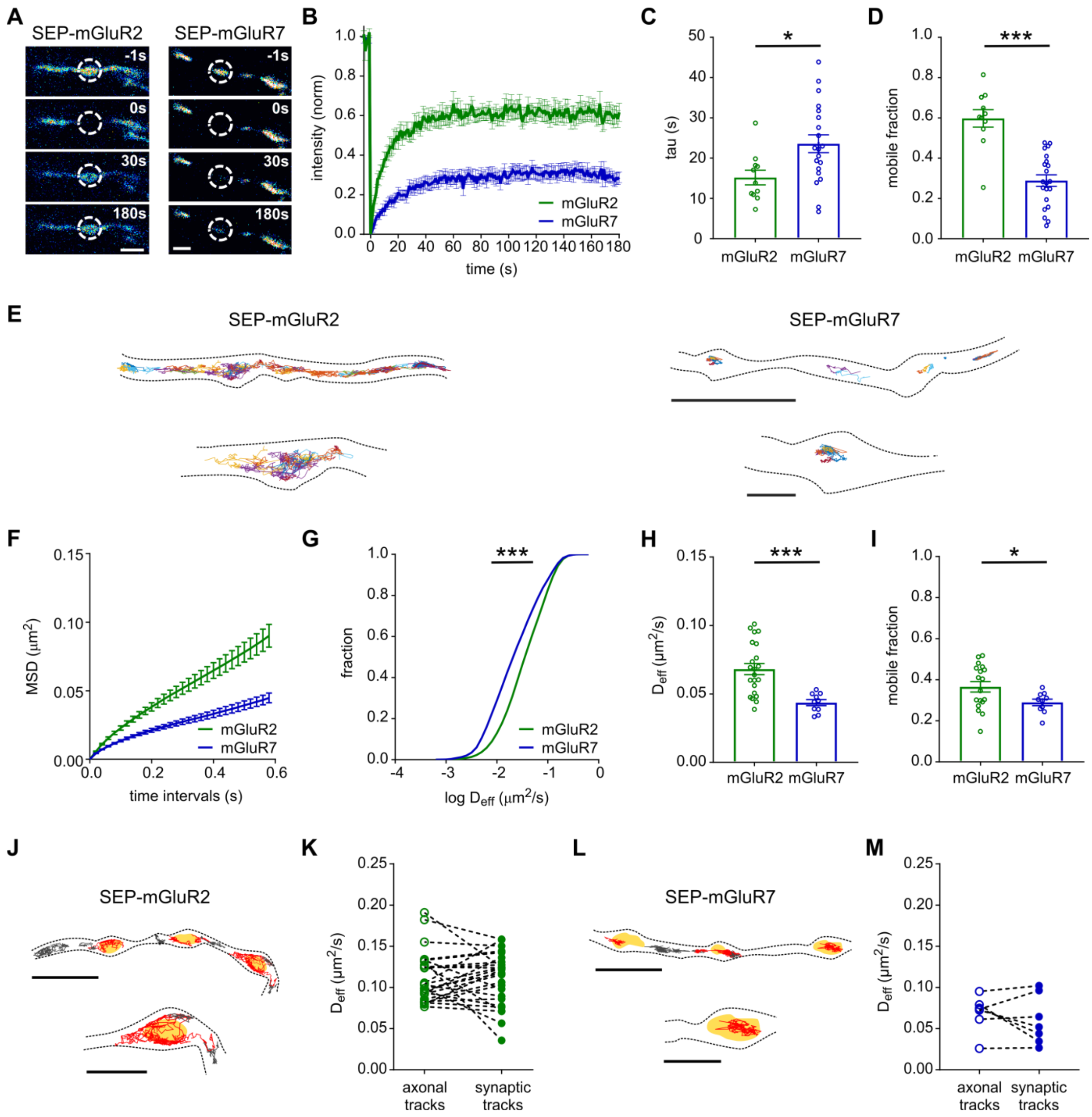


**Figure 2:** Distinct surface diffusion behavior of mGluR2 and mGluR7**. (A)** Example images from a FRAP time series in neurons expressing SEP-mGluR2 and SEP-mGluR7. The dotted circles indicate the bleached boutons. Scale bar, 1 µm. **(B)** Normalized fluorescence recovery of SEP-mGluR2 and SEP-mGluR7 (n = 11 boutons for SEP-mGluR2, 21 boutons for SEP-mGluR7 from 2 independent experiments). **(C)** and **(D)** Quantification of half time of fluorescence recovery (**C**) and mobile fraction (**D**) of SEP-tagged mGluRs. Unpaired *t*-test, * *P<0.05*, *** *P<0.0005*. Error bars represent SEM. **(E)** Example trajectories of SEP-mGluR2 and SEP-mGluR7. Trajectories are displayed with random colors. Outlines of cells are based on TIRF image of SEP signal. Scale bar, 5 µm; zooms, 1 µm. **(F)** Average mean square displacement (MSD) plot of SEP-mGluR2 and SEP-mGluR7 (n = 22 fields of view for mGluR2, 10 fields of view form mGluR7 from 3 independent experiments). **(G)** Frequency distribution of instantaneous diffusion coefficient ($D_{eff}$) of SEP-mGluR2 and SEP-mGluR7 (n = 22,821 trajectories for SEP-mGluR2, 5,161 trajectories for SEP-mGluR7). Kolmogornov-Smirnov test; *** *P<0.0001*. **(H)** and **(I)** Quantification of the average instantaneous diffusion coefficient ($D_{eff}$) (**H**) and mobile fraction (**I**) of SEP-tagged mGluRs (n = 22 fields of view for mGluR2, 10 fields of view for mGluR7 from 3 independent

experiments). Unpaired *t*-test; * *P<0.05*, *** *P<0.0005*. Error bars represent SEM. **(J)** Trajectories of SEP-mGluR2 plotted on top of the mask marking the presynaptic bouton. Red tracks - synaptic tracks, grey tracks - axonal tracks, yellow areas - bouton mask based on Syp-mCherry signal. Scale bar, 2 µm; zooms, 1 µm. **(K)** Quantification of the instantaneous diffusion coefficient ($D_{eff}$) of axonal and synaptic tracks of SEP-mGluR2 (n = 27 fields of view from 2 independent experiments). **(L)** Trajectories of SEP-mGluR7 plotted on top of the mask marking the presynaptic bouton, as in **(J)**. **(M)** Quantification of instantaneous diffusion coefficient ($D_{eff}$) of axonal and synaptic tracks of SEP-mGluR7 (n = 7 fields of view from 2 independent experiments).

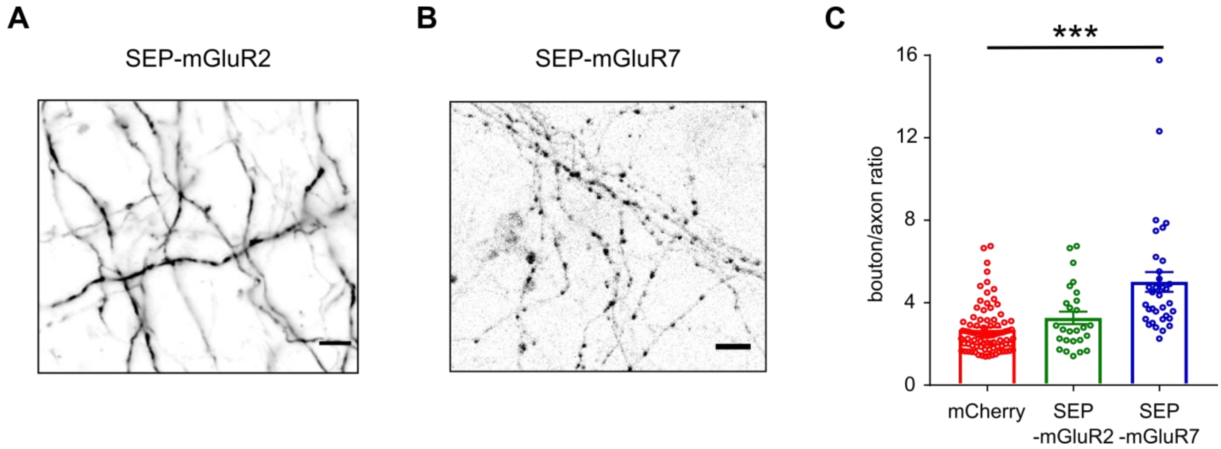


**Figure supplement 2.** Targeting of SEP-tagged mGluRs. **(A)** Example confocal image of neurons expressing SEP-mGluR2. Scale bar, 5 µm. **(B)** Example confocal image of neurons expressing SEP-mGluR7. Scale bar, 5 µm. **(C)** Quantification of ratios of fluorescence intensity in bouton over axon (n = 84 boutons for mCherry, 26 boutons for SEP-mGluR2, 34 boutons for SEP-mGluR7 from 2 independent experiments). The apparent increase in bouton/axon ratio of cytosolic mCherry likely results from larger bouton volume compared to axon. One-way ANOVA followed by Dunnett's multiple comparisons test, *** *P<0.001*.

## Single-molecule tracking reveals differences in diffusional behavior of mGluR2 and mGluR7

To resolve the dynamics of mGluR2 and mGluR7 at high spatial resolution and to investigate whether the diffusional behavior of these receptors is heterogeneous within axons, we next performed live-cell single-molecule tracking experiments using universal point accumulation in nanoscale topography (uPAINT) (Giannone et al., 2010). SEP-tagged receptors were labeled with anti-GFP nanobodies conjugated to ATTO-647N at low concentrations, which allowed to reliably detect, localize, and track single receptors over time for up to several seconds. The acquired receptor tracks were then compiled into trajectory maps revealing the spatial distribution of receptor motion. These maps were consistent with the receptor distribution patterns as resolved with gSTED imaging. SEP-mGluR2 seemed to rapidly diffuse throughout the axon and synaptic boutons, while SEP-mGluR7 motion was limited and highly confined within synaptic boutons with only a few molecules occasionally diffusing along the axon shaft (Figure 2E). The mean squared displacement (MSD) vs. elapsed time curves (Figure 2F) display a sublinear relationship for both receptor types indicating that the majority of these receptors undergo anomalous diffusion. The instantaneous diffusion coefficients ($D_{eff}$) for both receptors was estimated by fitting the slope through the four initial points of the MSD curves. Histograms of $D_{eff}$ estimated from individual trajectories (Figure 2G) and the average $D_{eff}$ per field of view (Figure 2H) revealed a significantly higher diffusion coefficient for SEP-mGluR2 than for SEP-mGluR7 ($D_{eff}$ SEP-mGluR2: 0.068 ± 0.004 $\mu m^2/s$, SEP-mGluR7: 0.044 ± 0.002 $\mu m^2/s$, $P<0.0005$, unpaired *t*-test), further indicating that mGluR2 diffuses much more rapidly in the axonal membrane than mGluR7. In addition, we classified the receptors diffusional states as either mobile or immobile in a manner independent of MSD-based diffusion coefficient estimation, i.e. by determining the ratio between the radius of gyration and the mean displacement per time step of individual trajectories (Golan and Sherman, 2017). Using this approach, we found that SEP-mGluR2 showed a higher fraction of mobile tracks than SEP-mGluR7 (mobile fraction SEP-mGluR2: 0.37 ± 0.03, SEP-mGluR7: 0.29 ± 0.02, $P<0.05$, unpaired *t*-test; Figure 2I) further confirming that in axons, mGluR2 is overall more mobile than mGluR7.

To determine whether the surface mobility of these receptors is differentially regulated at synaptic sites, we co-expressed SEP-tagged mGluRs together with a marker of presynaptic boutons, Synaptophysin1 (Syp1) fused to mCherry. Based on epifluorescence images of Syp1-mCherry, we created a mask of presynaptic boutons and compared the $D_{eff}$ of receptors diffusing inside or outside synapses (Figure 2J, L). The diffusion coefficient of SEP-mGluR2 within presynaptic boutons and along axons did not differ significantly ($D_{eff}$ axonal tracks: 0.113 ± 0.006 $\mu m^2/s$, $D_{eff}$ synaptic tracks: 0.110 ± 0.006 $\mu m^2/s$, $P>0.05$, paired *t*-test ; Figure 2J, K), suggesting that mGluR2 diffusion is not hindered at synaptic sites. Comparing the diffusion coefficients of the few axonal SEP-mGluR7 tracks with synaptic tracks showed that at a subset of synapses the mobility of SEP-mGluR7 is considerably lower inside boutons. However, we could not detect a significant difference in diffusion coefficient between synaptic and extrasynaptic SEP-mGluR7 ($D_{eff}$ axonal tracks: 0.069 ± 0.008 $\mu m^2/s$, $D_{eff}$ synaptic tracks: 0.060 ± 0.011 $\mu m^2/s$, $P>0.05$, paired *t*-test; Figure 2L, M). Taken together, the FRAP and single-molecule tracking data indicate a striking difference in the dynamic behavior of presynaptic mGluRs. mGluR2 diffuses seemingly unhindered throughout the axon, while mGluR7 is largely immobilized, preferentially at presynaptic active zones.

**The intracellular domain of mGluR2 regulates receptor mobility**

To gain insight into the structural mechanisms that control the dynamics of presynaptic mGluRs and to explain the distinct diffusional properties of mGluR2 and mGluR7, we next sought to identify the receptor domains that are involved in controlling mGluR mobility. mGluRs consist of three regions: the intracellular domain (ICD) containing a PDZ binding motif, the prototypical seven-helix transmembrane domain (TMD) involved in G-protein coupling and the large extracellular domain (ECD) that includes the ligand-binding site (Niswender and Conn, 2010). First, to unravel which segment of mGluR2 regulates its mobility, we created three chimeric receptors of mGluR2 by exchanging the ICD, TMD or ECD domains of mGluR2 with the corresponding domains of mGluR7 to maintain the overall structure of the receptor. All SEP-tagged chimeric mGluR2 variants were targeted to the axon, similar as wild-type mGluR2, indicating that axonal targeting and surface expression were not altered by replacing these domains (Figure 3 - figure supplement 3A). Moreover, single-molecule tracking showed that all chimeric mGluR2 variants displayed rapid diffusion throughout the axon and presynaptic boutons, similar to wild-type mGluR2 (Figure 3A). Interestingly though, the mGluR2 chimera containing the ICD of mGluR7 revealed a significantly higher diffusion coefficient compared to wild-type mGluR2 ($D_{eff}$ SEP-mGluR2-ICD7: 0.082 ± 0.003 $\mu m^2/s$, SEP-mGluR2: 0.065 ± 0.003 $\mu m^2/s$, $P<0.005$, one-way ANOVA), while exchanging the TMD or ECD did not affect the diffusion kinetics of mGluR2 ($D_{eff}$ SEP-mGluR2-TMD7: 0.063 ± 0.004 $\mu m^2/s$; SEP-mGluR2-ECD7: 0.067 ± 0.003 $\mu m^2/s$, $P>0.05$, one-way ANOVA; Figure 3B). Thus, comparing the diffusional behavior of this set of chimeric mGluR2 variants indicates that intracellular interactions mediate mGluR2 mobility in axons.

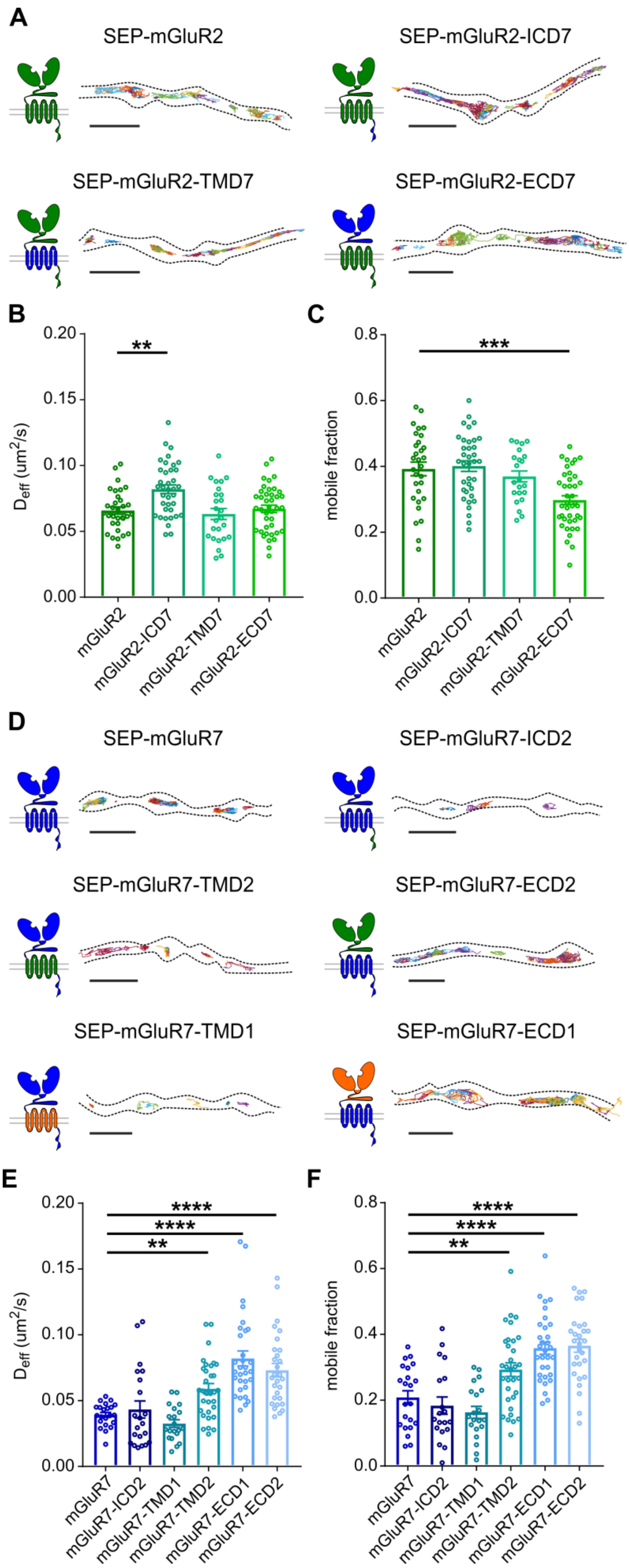


**Figure 3:** Distinct intra- and extracellular interactions regulate mobility of presynaptic mGluRs. **(A)** Schematic diagrams and example trajectories of wild-type and chimeric variants

of mGluR2 (green) with the ICD, TMD and ECD exchanged with the corresponding mGluR7 domains (blue). Scale bar, 2 µm. **(B)** and **(C)** Quantification of average diffusion coefficient ($D_{eff}$) (**B**) and mobile fraction (**C**) of SEP-tagged chimeric mGluR2 variants (n = 30 - 40 fields of view from 4 - 5 independent experiments). One-way ANOVA followed by Dunnett's multiple comparisons test; ** $P<0.005$, *** $P<0.0005$. Error bars represent SEM. **(D)** Schematic diagrams and example trajectories of wild-type and chimeric variants of mGluR7 (blue) with the ICD, TMD and ECD exchanged with the corresponding domains from mGluR2 (green) or mGluR1 (orange). Scale bar, 2 µm. **(E)** and **(F)** Quantification of average diffusion coefficient ($D_{eff}$) (**E**) and mobile fraction (**F**) of SEP-tagged chimeras of mGluR7 (n = 22 - 32 fields of view from 4 - 5 independent experiments). One-way ANOVA followed by Dunnett's multiple comparisons test; ** $P<0.05$, **** $P<0.0005$. Error bars represent SEM. All trajectories are displayed with random colors. Outlines of cells are based on TIRF image of SEP signal.

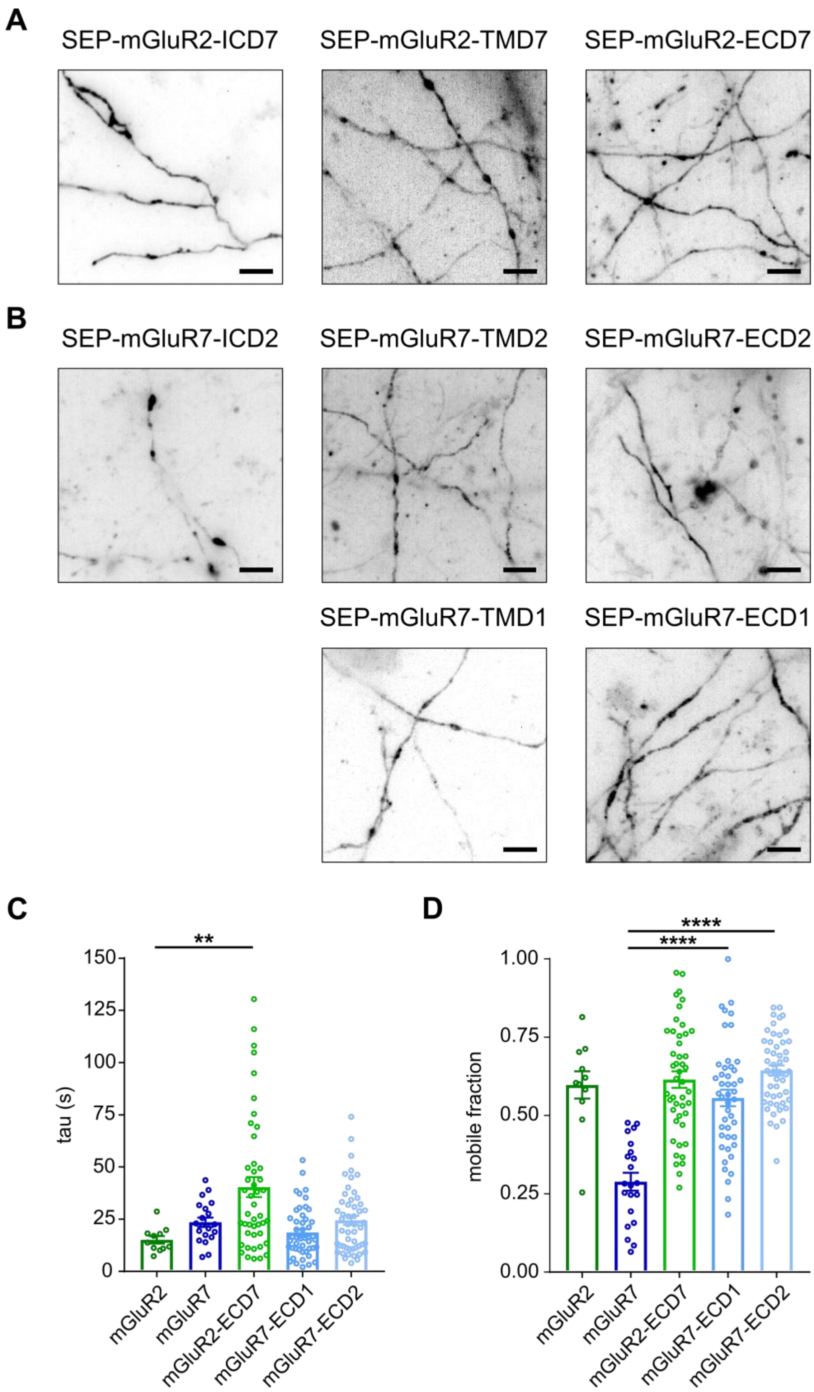


**Figure supplement 3.** Expression of chimeric variants of presynaptic mGluRs and FRAP experiments of extracellular chimeric receptors. **(A)** Example images of neurons expressing SEP-tagged chimeric mGluR2 variants. Scale bar, 5 µm. **(B)** Example images of neurons expressing SEP-tagged chimeric mGluR7 variants. Scale bar, 5 µm. **(C and D)** Quantification of half time of fluorescence recovery **(C)** and mobile fraction **(D)** from FRAP experiments of SEP-tagged extracellular chimeric variants of mGluR2 and mGluR7 (n = 10 - 45 boutons from 2 - 3 independent experiments). Kruskal-Wallis ANOVA in **(C)**; one-way ANOVA in **(D)** followed by Dunnett's multiple comparisons test ** *P<0.05*, **** *P<0.0005*. Error bars represent SEM.

**mGluR7 stability at presynaptic active zones is controlled by extracellular interactions**

While mGluR2 rapidly diffuses through the axon, we found that mGluR7 is stably anchored and concentrated at active zones. Therefore, we decided to further focus on the mechanisms that could underlie the immobilization of mGluR7 at presynaptic sites. To test which region of mGluR7 is involved in the immobilization of mGluR7 at the active zone, we generated five chimeric variants of mGluR7 to exchange the ICD, TMD or ECD of mGluR7 with the corresponding domains of mGluR2 or mGluR1. Because the C-terminal domain of mGluR1 is involved in targeting the receptor to the dendritic compartment we decided to not substitute the ICD of mGluR7 for the ICD of mGluR1 (Francesconi and Duvoisin, 2002). All SEP-tagged chimeric variants of mGluR7 were readily detected in axons, similar to wide-type mGluR7 (Figure 3 - figure supplement 3B) indicating that these receptors are correctly targeted to the axonal membrane.

In contrast to mGluR2, exchange of the ICD of mGluR7 did not change the diffusional behavior of the receptor. Trajectory maps obtained from single-molecule tracking showed that diffusion of the SEP-tagged mGluR7 chimera containing the ICD of mGluR2 was still restricted to presynaptic boutons (Figure 3D) and the diffusion coefficient ($D_{eff}$ SEP-mGluR7-ICD2: 0.043 ± 0.004 $\mu m^2/s$ , SEP-mGluR7: 0.039 ± 0.002 $\mu m^2/s$, $P>0.05$, one-way ANOVA; Figure 3E) and mobile fraction were similar to wild-type SEP-mGluR7 (mobile fraction SEP-mGluR7-ICD2: 0.18 ± 0.03, SEP-mGluR7: 0.21 ± 0.02, $P>0.05$, one-way ANOVA; Figure 3F), suggesting that intracellular interactions do not contribute to mGluR7 immobilization. Diffusion of SEP-tagged TMD chimeric variants of mGluR7 was also mostly restricted to presynaptic boutons (Figure 3D), although we found that replacing the mGluR7 TMD with the TMD of mGluR2 slightly increased the diffusion coefficient ($D_{eff}$: SEP-mGluR7-TMD2 0.059 ± 0.004 $\mu m^2/s$, $P<0.05$, one-way ANOVA; Figure 3E) and mobile fraction (SEP-mGluR7-TMD2 0.29 ± 0.02, $P<0.05$, one-way ANOVA; Figure 3F). However, substitution of the mGluR7 TMD with the mGluR1 TMD did not alter its diffusional behavior ($D_{eff}$ SEP-mGluR7-TMD1: 0.033 ± 0.003 $\mu m^2/s$, mobile fraction: 0.16 ± 0.02, $P>0.05$, one-way ANOVA; Figure 3E, F), suggesting that the faster diffusion of the mGluR7 variant containing the TMD of mGluR2 is most likely due to specific properties of the mGluR2 TMD and cannot be attributed to a mGluR7-specific mechanism. Indeed, a previous study reported stronger interactions between transmembrane regions in mGluR2 homodimers compared to other mGluR subtypes (Gutzeit et al., 2019).

Interestingly, replacing the ECD of mGluR7 drastically altered its diffusional behavior. In contrast to the wild-type receptor, SEP-tagged chimeric mGluR7 variants containing the ECD of mGluR2 or mGluR1 diffused freely throughout the axon and boutons (Figure 3D) and displayed almost a two-fold increase in diffusion coefficient ($D_{eff}$ SEP-mGluR7-ECD1: 0.082 ± 0.006 $\mu m^2/s$, SEP-mGluR7-ECD2: 0.073 ± 0.005 $\mu m^2/s$, $P<0.0005$, one-way ANOVA; Figure 3E) and larger mobile fraction compared to wild-type SEP-mGluR7 (SEP-mGluR7-ECD1: 0.36 ± 0.02, SEP-mGluR7-ECD2: 0.37 ± 0.02, SEP-mGluR7: 0.21 ± 0.02, $P<0.0005$, one-way ANOVA; Figure 3F). Thus, the immobilization of mGluR7 at presynaptic sites likely relies on extracellular interactions with its ECD. To assess if the ECD of mGluR7 is sufficient to immobilize receptors, we replaced the ECD of mGluR2 with the ECD of mGluR7. Indeed, we found a significant decrease in the mobile fraction of the SEP-tagged chimeric mGluR2 variant containing the mGluR7 ECD (SEP-mGluR2-ECD7: 0.30 ± 0.02, SEP-mGluR2: 0.39 ± 0.02, $P<0.0005$, one-way ANOVA; Figure 3C) supporting the role of the mGluR7 ECD in immobilizing the receptor at synaptic sites. To further substantiate these results, we performed FRAP experiments and found a significant increase in fluorescence recovery of SEP-tagged mGluR7 variants with substituted ECDs (Figure 3 - figure supplement 3D) and slower recovery kinetics of SEP-tagged chimeric mGluR2 with the ECD of mGluR7 (Figure 3 - figure supplement 3C). These results are in striking agreement with the single-molecule tracking data and confirm the dominant role of the mGluR7 ECD in regulating receptor mobility.

**The adhesion molecule ELFN2 interacts with the extracellular domain of mGluR7 in *trans***

Given the large contribution of the ECD of mGluR7 to surface mobility, we sought to gain further insights in the ECD-mediated interactions that could underlie the anchoring of mGluR7 at presynaptic boutons. It was recently shown that the postsynaptic adhesion molecules ELFN1 and ELFN2 can interact transsynaptically with mGluR7 and modulate its activity (Dunn et al., 2019b; Tomioka et al., 2014). Since ELFN1 expression seems restricted to inhibitory neurons (Stachniak et al., 2019; Sylwestrak and Ghosh, 2012), we hypothesized that a potential transsynaptic interaction between mGluR7 and the widely expressed ELFN2 (Dunn et al., 2019b) could anchor mGluR7 at presynaptic sites. To further investigate this hypothesis, we first assessed whether ELFN2 is expressed in hippocampal neurons. Immunostaining for ELFN2 revealed a punctate distribution pattern (Figure 4 - figure supplement 4A), with ELFN2-positive puncta co-localizing with the postsynaptic density marker PSD-95 (Figure 4A, B), adjacent to presynaptic active zones marked by Bsn (Figure 4C, D). Confirming this finding, we obtained similar distribution patterns using endogenous GFP-tagged ELFN2 (Figure 4 - figure supplement 4B-D). Additionally, we found that endogenous ELFN2-postive clusters co-localized with mGluR7-positive puncta (Figure 4 - figure supplement 4E). Then, to test whether mGluR7 can be recruited and clustered by ELFN2, we co-cultured a population of U2OS cells transfected with mOrange-tagged mGluR7 with a population of cells expressing ELFN2-GFP to detect possible interactions in *trans* between these proteins at the junctions between the two populations of transfected cells. We observed a strong accumulation of both mGluR7 and ELFN2 at the interfaces between cells expressing mOrange-mGluR7 and ELFN2-GFP (Figure 4F). In contrast, we did not find recruitment of mOrange-mGluR2 to junctions with ELFN2-expressing cells (Figure 4E), suggesting that trans interactions with ELFN2 can indeed specifically recruit mGluR7, in line with recent findings (Dunn et al., 2019b). To further investigate if this interaction is mediated by the extracellular domain of mGluR7, we tested whether replacing the mGluR2 ECD with the mGluR7 ECD would be sufficient to recruit mGluR2 to the junctions with ELFN2 expressing cells. Indeed, mGluR2 harboring the ECD of mGluR7 was strongly recruited to the junctions with ELFN2 expressing cells (Figure 4G). These results indicate that ELFN2 can potently recruit mGluR7 to cellular junctions and that the ECD of mGluR7 is both required and sufficient for receptor recruitment by ELFN2.

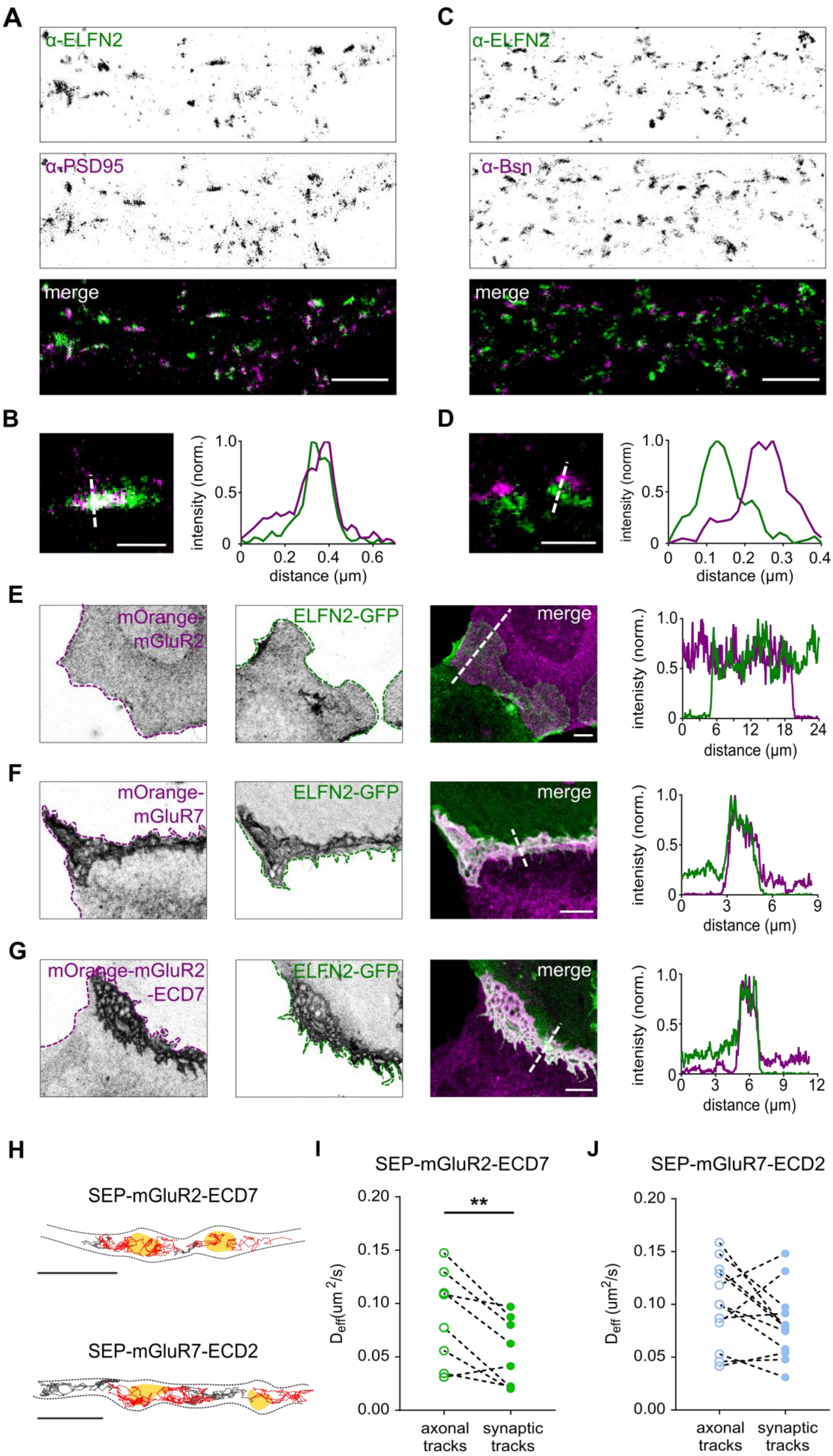


**Figure 4:** Postsynaptic adhesion molecule ELFN2 interacts with the extracellular domain of mGluR7. **(A)** gSTED image of neuron co-stained with anti-ELFN2 (STAR580) and anti-PSD95 (STAR635P). Scale bar, 2 μm. **(B)** Example image and intensity profile of individual ELFN2-positive synapse from **(A)**. Scale bar, 500 nm. **c** gSTED image of neuron co-stained

with anti-ELFN2 (STAR580) and anti-Bsn (STAR635P). Scale bar, 2 µm. **(D)** Example image and intensity profiles of individual ELFN2 positive synapse from **(C)** Scale bar, 500 nm. **(E - G)** Example images of mixed co-cultures of U2OS cells expressing ELFN2-GFP and mOrange-mGluR2 (**E**), mOrange-mGluR7 (**F**), mOrange-mGluR2-ECD7 (**G**) and normalized intensity profiles along interface between cells expressing different proteins indicated with dashed lines. Dotted line - outline of cell. Scale bar, 10 µm. **(H)** Trajectories of extracellular chimeras SEP-mGluR2-ECD7 and SEP-mGluR7-ECD2 plotted on the top of mask of presynaptic bouton. Red tracks - synaptic tracks, grey tracks - axonal tracks, yellow areas - bouton mask based on Syp-mCherry signal. Scale bar, 2 µm. **(I)** and **(J)** Quantification of diffusion coefficient ($D_{eff}$) of axonal and synaptic tracks of SEP-mGluR2-ECD7 (**I**) and SEP-mGluR7-ECD2 (**J**) (n = 8 fields of view for SEP-mGluR2-ECD7, 12 fields of view for SEP-mGluR7-ECD2 from 2 independent experiments). Paired *t*-test, ** *P<0.005*.

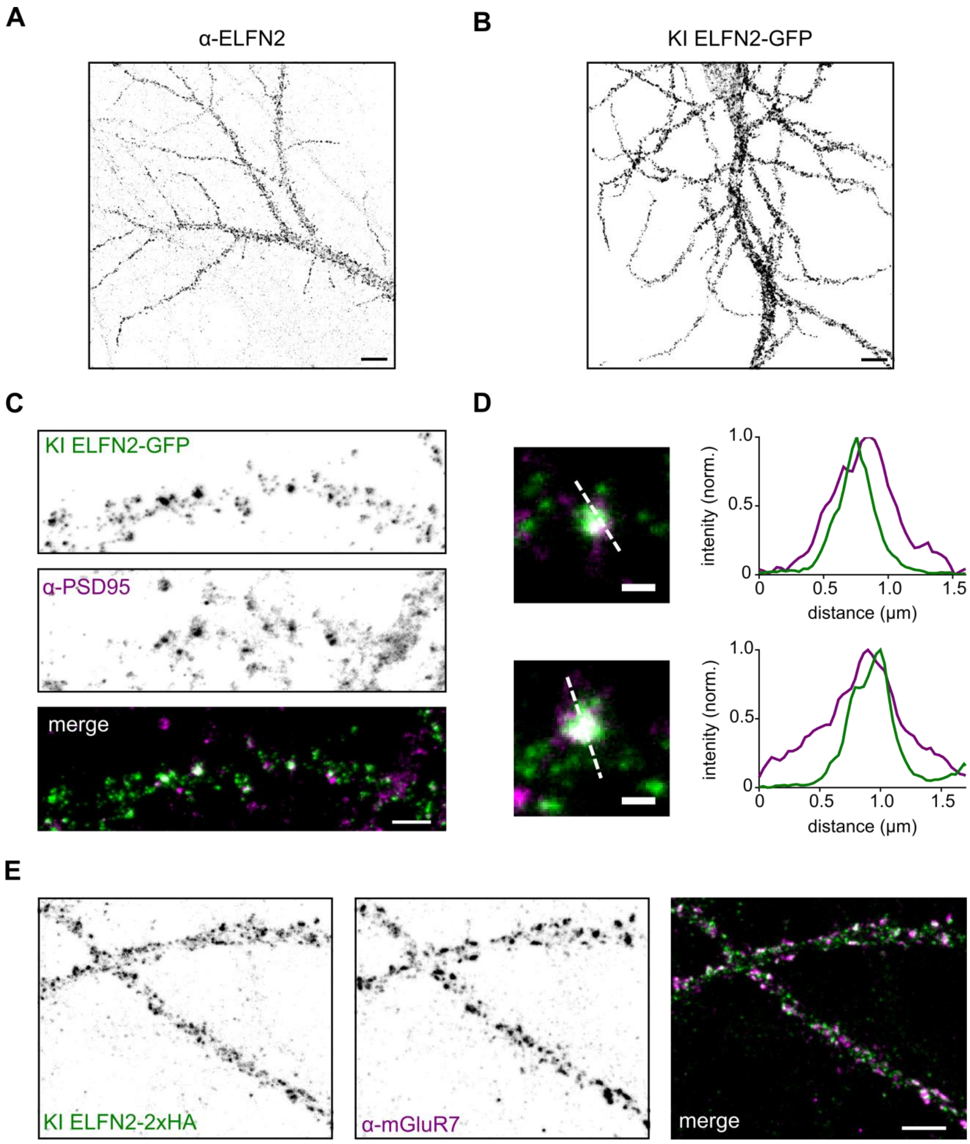


**Figure supplement 4.** Distribution of ELFN2. **(A)** Example confocal image of neuron stained with anti-ELFN2 (STAR580). Scale bar, 10 µm. **(B)** Example confocal image of ELFN2-GFP CRISPR/Cas9 knock-in neuron. GFP signal was enhanced with anti-GFP (STAR580). Scale bar, 10 µm **(C)** gSTED image of neuron ELFN2-GFP CRISPR/Cas9 knock-in neuron co-stained with anti-PSD95 (STAR635P). Scale bar, 2 µm. **(D)** Example images and intensity profiles of individual ELFN2-positive synapses from **(C)**. Scale bar, 500 nm. **(E)** Confocal image of ELFN2-2xHA CRISPR/Cas9 knock-in neuron stained with anti-mGluR7 (STAR635P) antibodies. HA-tag was visualized with anti-HA (Alexa Fluor 594) antibodies. Scale bar, 5 μm.

**The extracellular domain of mGluR7 instructs immobilization at the active zone**

Based on our findings that the localization of mGluR7 is restricted to the active zone and that the ECD of mGluR7 can interact with the postsynaptic adhesion molecule ELFN2, we hypothesized that the ECD of mGluR7 mediates receptor immobilization specifically at presynaptic sites. To test this hypothesis, we resolved receptor mobility at synapses by co-expressing ECD chimeric variants of mGluR2 and mGluR7 with Syp1-mCherry (Figure 4H). Although the mGluR2 chimera containing the ECD of mGluR7 displayed rather high diffusion coefficients in the axonal shaft (Figure 3B), the pool of chimeric receptors inside presynaptic boutons showed a significantly lower diffusion coefficient ($D_{eff}$ synaptic tracks: $0.054 \pm 0.011$ μm$^2$/s, axonal tracks: $0.087 \pm 0.015$ μm$^2$/s, $P<0.005$, paired $t$-test; Figure 4I). Vice versa, replacing the ECD of mGluR7 for the ECD of mGluR2 resulted in a similar diffusion coefficient of axonal and synaptic tracks ($D_{eff}$ synaptic tracks: $0.081 \pm 0.01$ μm$^2$/s, axonal tracks: $0.1 \pm 0.01$ μm$^2$/s, $P>0.05$, paired $t$-test; Figure 4J) suggesting that the ECD of mGluR7 is indeed sufficient to immobilize receptors at presynaptic sites. Altogether, these results indicate that mGluR7 immobilization at synaptic sites is in large part mediated by extracellular interactions.

**Surface mobility of presynaptic mGluRs is not altered by synaptic activity**

Our results so far suggest that, under resting conditions, the diffusional properties of presynaptic mGluRs are largely controlled by distinct intra- and extracellular interactions. However, ligand-induced activation of GPCRs involves a dramatic change in receptor conformation, and has been shown to change the oligomerization and diffusion behavior of various GPCRs, including mGluRs, in non-neuronal cells (Calebiro et al., 2013; Kasai and Kusumi, 2014; Sungkaworn et al., 2017; Yanagawa et al., 2018). To test whether receptor activation alters the diffusion of presynaptic mGluRs in neurons, we performed single-molecule tracking of mGluR2 and mGluR7 before and after stimulation with their specific agonists. We found that activation of SEP-mGluR2 with the potent agonist LY379268 (LY) did not change the distribution of receptor trajectories (Figure 5A) or diffusion coefficients ($D_{eff}$ control: 0.06 ± 0.003 $\mu m^2/s$, LY: 0.058 ± 0.004 $\mu m^2/s$, $P$>0.05, paired *t*-test; Figure 5B). Similarly, direct activation of mGluR7 with the potent group III mGluR agonist L-AP4 also did not change the diffusional behavior of SEP-mGluR7 ($D_{eff}$ control: 0.044 ± 0.002 $\mu m^2/s$, L-AP4: 0.045 ± 0.003 $\mu m^2/s$; $P$>0.05, paired *t*-test; Figure 5C, D). Thus, these experiments indicate that in neurons, the dynamics of presynaptic mGluRs are not modulated by agonist-stimulated receptor activation.

Changes in neuronal activity could alter receptor mobility, either directly by receptor stimulation by their endogenous ligand glutamate, or perhaps indirectly through structural changes in synapse organization. To test this, we next determined whether strong synaptic stimulation by application of the potassium channel blocker 4-AP together with the glutamate reuptake blocker TBOA, to increase synaptic glutamate levels, changed receptor diffusion. However, we did not find a significant effect of synaptic stimulation on the diffusion coefficient of SEP-mGluR2 ($D_{eff}$ control: 0.085 ± 0.011 $\mu m^2/s$, 4-AP + TBOA: 0.069 ± 0.009 $\mu m^2/s$, $P$>0.05, paired t-test; Figure 5 - figure supplement 5A, B). Additionally, even under strong depolarizing conditions (25 mM $K^+$, 5 - 10 min), the diffusion coefficient of SEP-mGluR2 remained unaltered ($D_{eff}$ control: 0.082 ± 0.005 $\mu m^2/s$, 25 mM $K^+$: 0.074 ± 0.008 $\mu m^2/s$, $P$>0.05, paired *t*-test; Figure 5E, F). We found similar results for SEP-mGluR7 (data not shown). However, since the affinity of mGluR7 for glutamate is very low, in the range of 0.5 - 1 mM (Schoepp et al., 1999), we reasoned that the unaltered diffusion of mGluR7 during synaptic stimulation could be due to the incomplete activation of the receptor. Therefore, we analyzed the mobility of an mGluR7 mutant with a two-fold increased affinity for glutamate (mGluR7-N74K) (Kang et al., 2015) during strong depolarization. Importantly, we found that the diffusion rate of SEP-mGluR7-N74K was not significantly different from wild-type SEP-mGluR7 under control conditions ($D_{eff}$ SEP-mGluR7-N74K: 0.049 ± 0.005 $\mu m^2/s$, SEP-mGluR7: 0.039 ± 0.002 $\mu m^2/s$, $P>0.05$, unpaired *t*-test; Figure 5 - figure supplement 5C-E). However, despite having a two-fold higher affinity for glutamate, the diffusion kinetics of SEP-mGluR7-N74K remained unaltered under strong depolarizing conditions ($D_{eff}$ control: 0.056 ± 0.006 $\mu m^2/s$, 25 mM $K^+$: 0.044 ± 0.007 $\mu m^2/s$, $P>0.05$, paired *t*-test; Figure 5G, H). Altogether, these single-molecule tracking experiments demonstrate that the lateral diffusion of presynaptic mGluRs on the axonal membrane is not modulated by direct activation with ligands, or acute changes in neuronal activity.

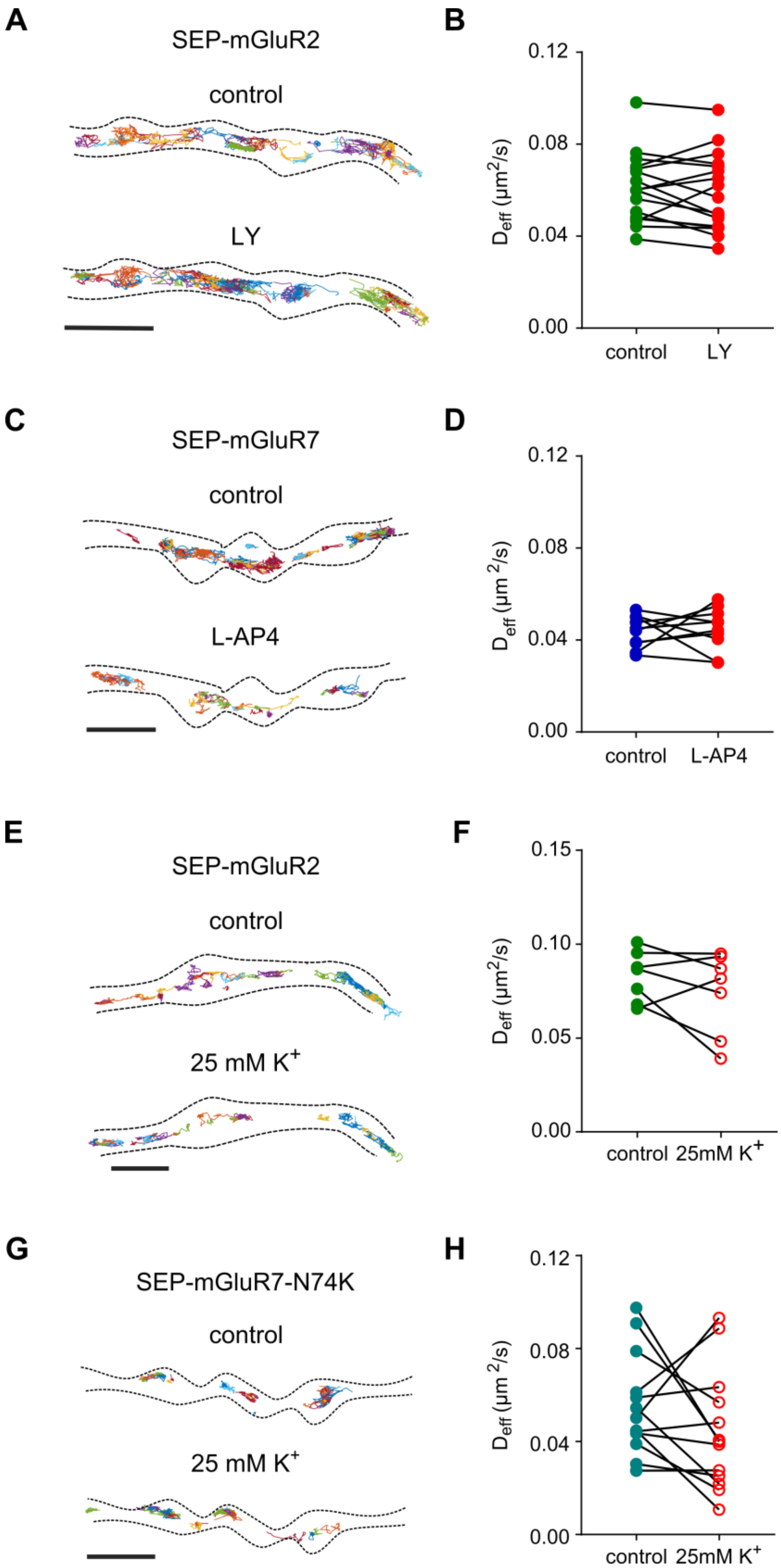


496

497 **Figure 5.** Dynamics of presynaptic mGluRs is not regulated by activity. **(A)** Example
498 trajectories of SEP-mGluR2 before and after incubation with 100 μM LY. Scale bar, 2 μm.
499 **(B)** Quantification of diffusion coefficient ($D_{eff}$) of SEP-mGluR2 before and after incubation
500 with LY (n = 17 fields of view from 2 independent experiments). **(C)** Example trajectories of
501 SEP-mGluR7 before and after incubation with 500 μM L-AP4. Scale bar, 2 μm.

**(D)** Quantification of diffusion coefficient ($D_{eff}$) of SEP-mGluR7 before and after incubation with L-AP4 (n = 10 fields of view from 2 independent experiments). **(E)** Example tracks of SEP-mGluR2 before and after incubation with 25 mM $K^+$. Scale bar, 2 µm. **(F)** Quantification of diffusion coefficient ($D_{eff}$) of SEP-mGluR2 before and after incubation with 25 mM $K^+$ (n = 7 fields of view from 2 independent experiments). **(G)** Example tracks of SEP-mGluR7-N74K before and after incubation with 25 mM $K^+$. Scale bar, 2 µm. **(H)** Quantification of diffusion coefficient ($D_{eff}$) of SEP-mGluR7-N74K before and after incubation and with 25 mM $K^+$ (n = 13 fields of view from 2 independent experiments). All trajectories are displayed with random colors. Outlines of cells are based on TIRF image of SEP signal.

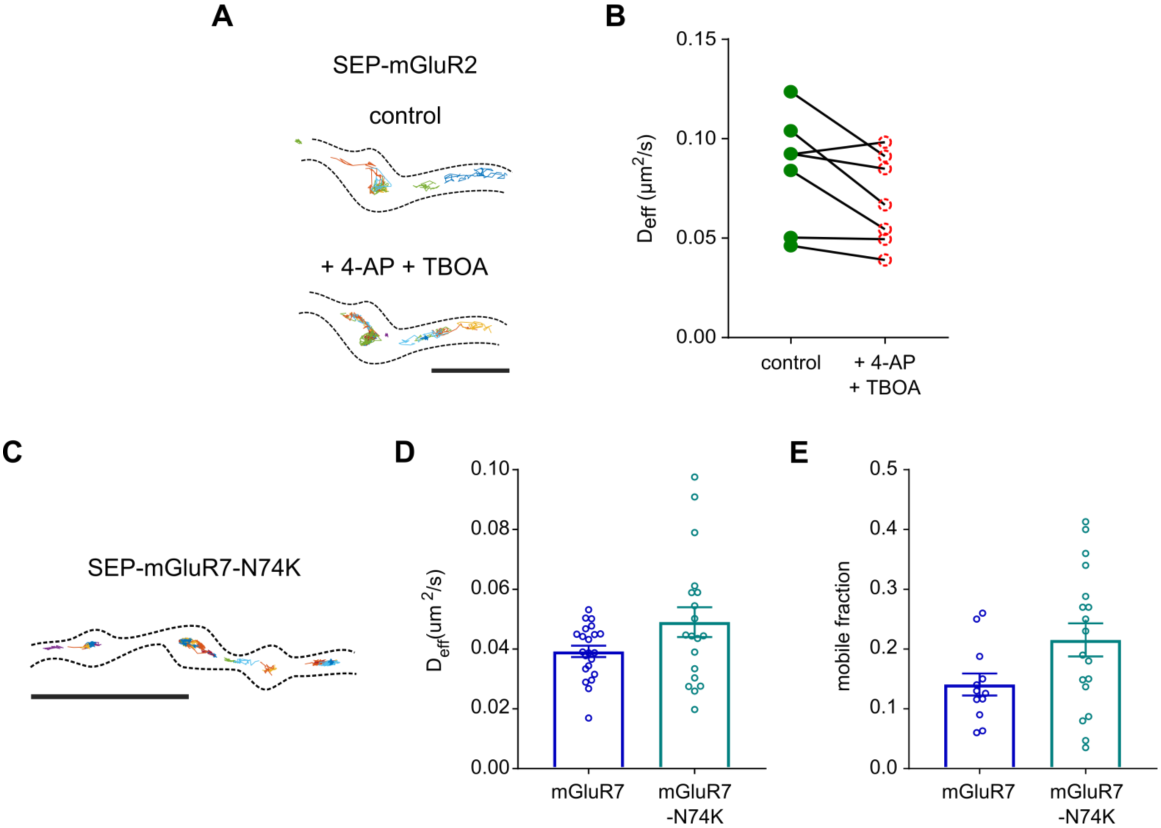


**Figure supplement 5.** Mobility of presynaptic mGluR2 does not depend of neuronal activity and high-affinity mutant of mGluR7 displays similar mobility as wild-type receptor. **(A)** Example tracks of SEP-mGluR2 before and after incubation with 200 µM 4-AP and 10 µM TBOA. Scale bar, 2 µm. **(B)** Quantification of diffusion coefficient ($D_{eff}$) of SEP-mGluR2 before and after incubation with 4-AP and TBOA (n = 7 fields of view from 2 independent experiments). **(C)** Example trajectories of SEP-mGluR7-N74K.. Scale bar, 5 µm. **(D and E)** Quantification of average diffusion coefficient ($D_{eff}$) **(D)** and mobile fraction **(E)** of SEP-mGluR7 and mutant SEP-mGluR7-N74K (n = 22 fields of views for SEP-mGluR7, 19 fields of view for SEP-mGluR7-N74K from 2 independent experiments). Trajectories are displayed with random colors. Outlines of cells is based on TIRF image of SEP signal. Error bars represent SEM.

**Computational model of presynaptic mGluR activation reveals that different levels of receptor activation depend on subsynaptic localization**

Our data show that mGluR7 is immobilized at the active zone, close to the release site, while mGluR2 is distributed along the axon and synaptic boutons, seemingly excluded from the active zone. Moreover, their localization and dynamics did not change upon synaptic activity. We hypothesized that these distinct distribution patterns differentially influence the contribution of presynaptic mGluRs to the modulation of synaptic transmission. To test this hypothesis, we investigated a computational model of presynaptic mGluR activation combining the cubic ternary complex activation model (cTCAM) of GPCRs signaling (Figure 6B) (Kinzer-Ursem and Linderman, 2007) with a model of time-dependent diffusion of glutamate release after single synaptic vesicle (SV) fusion or multi-vesicle release at different frequencies. To determine the effect of mGluR localization, we compared receptor activation at varying distances (5 nm to 1 μm) from the release site (Figure 6A). We calibrated the activation model of mGluR2 and mGluR7 by solving cTCAM with different values of association constant ($K_a$), keeping other parameters constant (Table supplement 1), to match the model outputs: the relative number of receptor-ligand complexes (Figure 6C) and the $G\alpha_{GTP}$ concentration (Figure 6D) with previously published $EC_{50}$ values for mGluR2 and mGluR7 (Schoepp et al., 1999). Because two out of four liganded receptor states in the cTCAM represent an inactive receptor, we used the $G_{\alpha GTP}$ concentration as a readout of receptor activation to compare responses of mGluRs to different synaptic activity patterns.

The release of glutamate from a single SV, representing release during spontaneous synaptic activity, caused only a slight increase in the activation of mGluR2 when located close to the release site (r = 5 nm) and outside the active zone (r ≥ 100 nm, Figure 6E and Figure 6 - figure supplement 6A). Release of 10 SVs, corresponding to the size of the readily releasable pool, at low frequency (5 Hz) increased the activity of mGluR2 almost 2-fold inside presynaptic boutons ($r \leq 500$ nm; Figure 6E and Figure 6 - figure supplement 6B). Elevation of the fusion frequency to 20 Hz further increased receptor activation to ~2.3-fold of basal activity (Figure 6E and Figure 6 - figure supplement 6C). Together, these data suggest that mGluR2 is activated during moderate synaptic stimulation patterns, in line with an earlier study suggesting use-dependent activation of group II mGluRs (Scanziani et al., 1997). Surprisingly, for all patterns of synaptic activity, levels of mGluR2 activation were almost identical next to the release site ($r = 5$ nm) and at the edge of the active zone ($r = 100$ nm) and only slowly decreased with increasing distance from the active zone ($r > 100$ nm, Figure 6E). These results suggest that mGluR2 is efficiently activated, even at further distances from the release site, and its activation is only loosely coupled to release site location. This finding is in line with the localization of mGluR2 along the axon and inside presynaptic bouton but not inside the active zone.

In contrast, mGluR7, having a distinctively low affinity for glutamate, was not efficiently activated by the release of single SV, even when positioned close to the release site. At $r = 5$ nm, we found less than 0.3% change in activation compared to basal receptor activity (Figure 6F and Figure 6 - figure supplement 6D). Release of 10 SVs at 5 Hz caused a relatively small increase (~ 1.5%) in mGluR7 activity (Figure 6F and Figure 6 - figure supplement 6E). However, fusion of the same number of SVs at higher frequency (20 Hz) almost doubled mGluR7 response to glutamate (~ 2.6% increase of $G_{\alpha GTP}$ concentration at $r = 5$ nm, Figure 6 - figure supplement 6F) suggesting that the level of mGluR7 activation strongly depends on the frequency of release and the peak of maximal glutamate concentration in the cleft. Additionally, the activity profiles of mGluR7 further away from the release site showed a striking reduction in mGluR7 response indicating that mGluR7 activation is mostly restricted to locations close release sites (Figure 6F). Altogether, these data indicate that mGluR7 is involved in modulation of synaptic transmission only during repetitive, high-frequency release and its localization at the active zone close to the release site is curtail for its function.

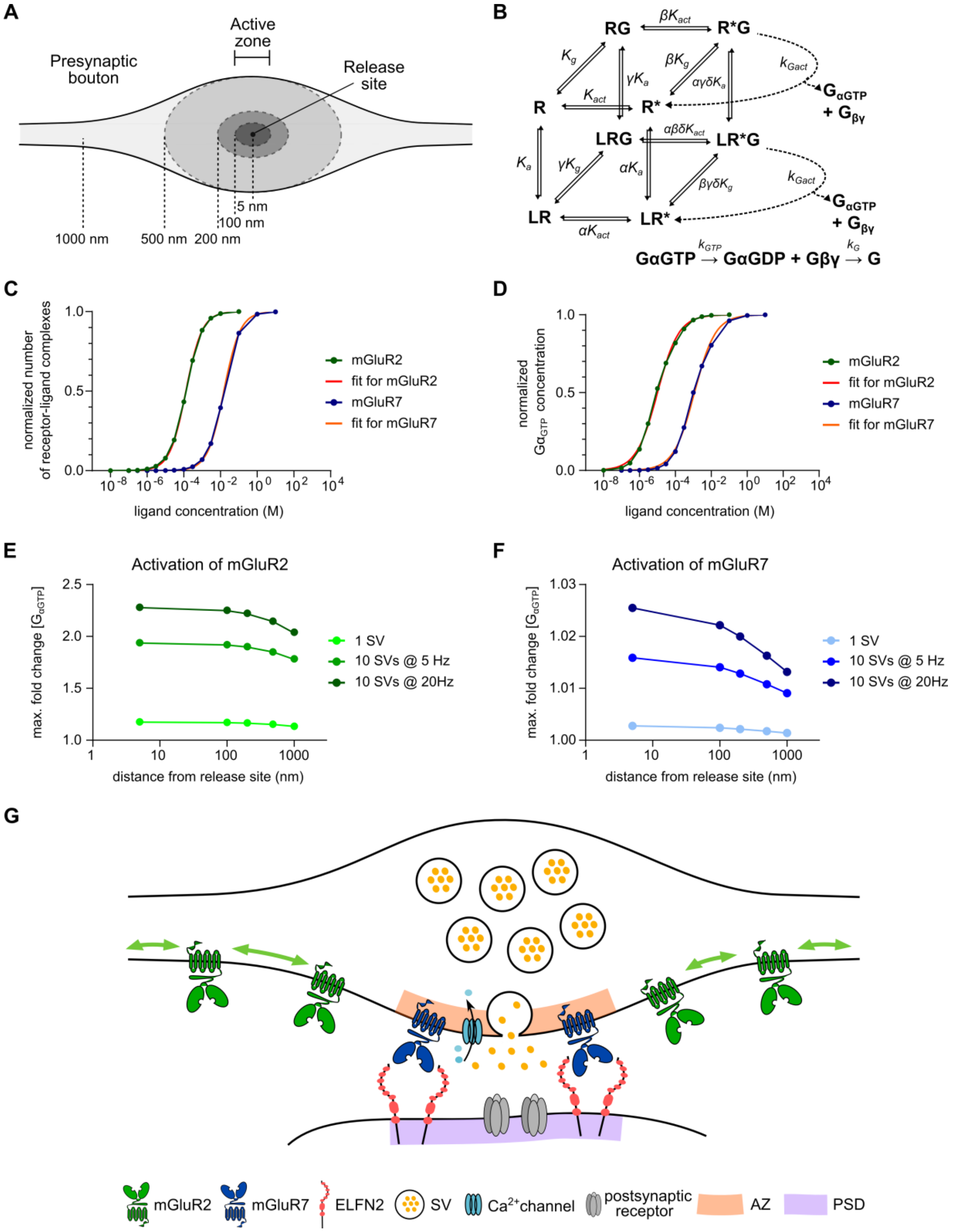


**Figure 6.** Computational model of mGluRs activation shows that subsynaptic localization of presynaptic mGluRs tunes receptor activation. **(A)** Schematic of presynaptic bouton

highlighting subsynaptic localizations used in modeling. **(B)** Kinetics and rate equations described in the cubic ternary complex activation model of presynaptic mGluRs signaling. All parameters used in the model are summarized in Table supplement 1. **(C)** and **(D)** Calibration of model to match output the number of receptor - ligand complexes (**C**) and $G\alpha_{GTP}$ concentration (**D**) with reported $EC_{50}$ values for mGluR2 and mGluR7. **(E)** and **(F)** Receptor response to glutamate release during different release pattern (1 SV, 10 SVs at 5 Hz and 10 SVs at 20 Hz) at different distances from release site (5 nm to 1 µm) for mGluR2 (**E**) and mGluR7 (**F**). Note that x axis is on a logarithmic scale. **(G)** Model of subsynaptic distribution and mobility of presynaptic mGluRs. mGluR2 is distributed along the axon and displays high mobility that is modulated by its intracellular interactions. mGluR7 is enriched and immobilized at the active zone. Immobilization of mGluR7 is regulated by its extracellular domain that transsynaptically interacts with the postsynaptic adhesion molecule ELFN2. SV - synaptic vesicle, AZ - the active zone, PSD - the postsynaptic density.

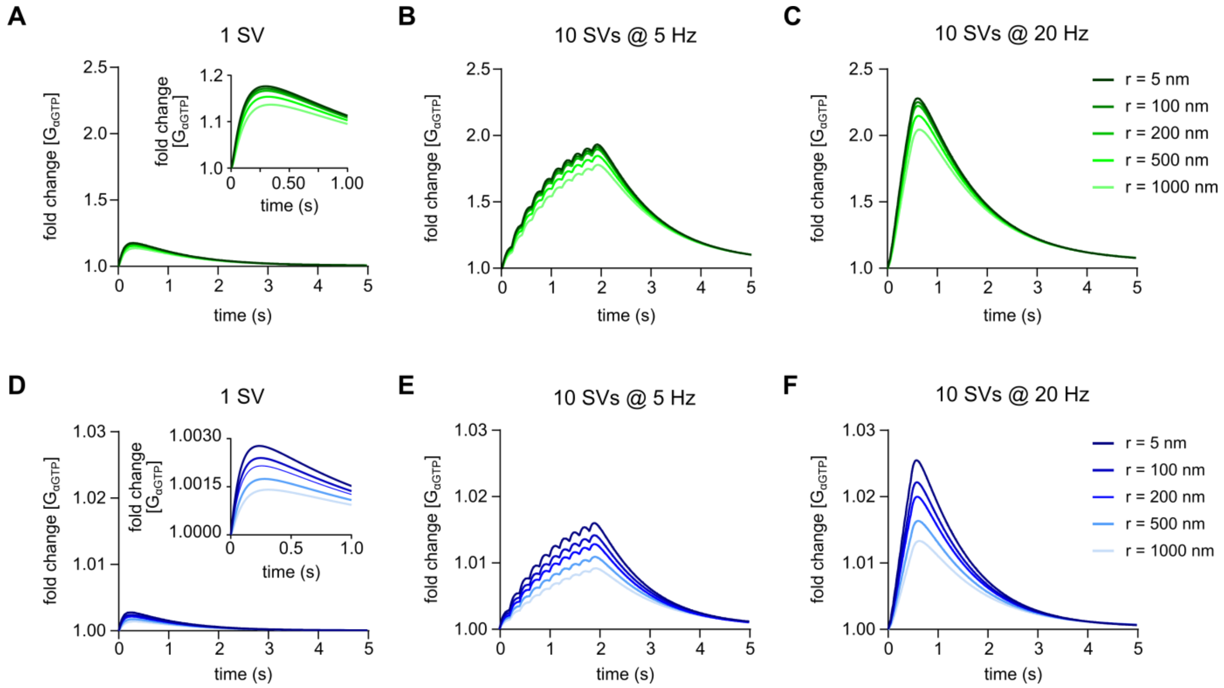


**Figure supplement 6.** mGluR2 activation is loosely coupled to the distance to the release site, while mGluR7 activation is restricted to close proximity of the release site. **(A - C)** Time courses of mGluR2 response to glutamate after release of 1 SV **(A)**, 10 SVs at 5 Hz **(B)** and 10 SVs at 20 Hz **(C)** at different distances from the release site. **(D - F)** Time courses of mGluR7 response to glutamate after release of 1 SV **(D)**, 10 SVs at 5 Hz **(E)** and 10 SVs at 20 Hz **(F)** at different distances from the release site.

## DISCUSSION

Despite the functional importance of presynaptic mGluRs in modulating the efficacy of synaptic transmission, the mechanisms that control their dynamic distribution at excitatory synapses remain poorly understood. Here, we provide new insights in the molecular mechanisms that determine the spatial distribution and mobility of presynaptic mGluRs (Figure 6G). We observed that presynaptic mGluR subtypes display striking differences in their subsynaptic localization and dynamics that are controlled by distinct structural mechanisms. We identified that the extracellular domain of mGluR7 is critical for immobilization of the receptor at presynaptic sites, which is likely mediated by transsynaptic interactions with the postsynaptic adhesion molecule ELFN2. Finally, a computational model of receptor activation showed that mGluR2 activation is only loosely coupled to release site location. In contrast, even when placed immediately next to the release site, there is only modest activation of mGluR7 by physiologically relevant synaptic stimulation patterns.

Mapping the precise distribution of presynaptic mGluRs is essential for understanding how these receptors contribute to synaptic transmission. In particular, the location relative to the release site is predicted to influence the probability of receptor activation and ability to trigger local downstream effectors. We found that while mGluR2 was distributed along the axon and in synaptic boutons it was largely excluded from the active zone. In contrast, we found that mGluR7 was highly enriched at the presynaptic active zone, close to the release site of synaptic vesicles. This is in line with earlier immuno-EM studies that showed that mGluR2 is present in the preterminal part of axons, but rarely found in boutons (Shigemoto et al., 1997), and that group III mGluRs, including mGluR7, are almost exclusively localized in the presynaptic active zone (Shigemoto et al., 1997, 1996; Siddig et al., 2020). Interestingly, these differences in localization were reflected in the surface diffusion behavior of these receptors. mGluR2 was highly mobile throughout the axon and within boutons, similar to other presynaptic receptors such as the cannabinoid type 1 receptor (CB1R) (Mikasova et al., 2008) and the mu-type opioid receptor (MOR) (Jullié et al., 2020). In contrast to these mobile receptors however, diffusion of mGluR7 was almost exclusively restricted to presynaptic boutons. Such differences in the distribution of presynaptic receptors are likely associated with their function and may provide a means for synapses to spatially and temporally compartmentalize receptor signaling.

The differences in the distance of these mGluR2 and mGluR7 to the release site implies that these receptors respond differentially to synaptic activity. Indeed, our computational modeling studies indicate that mGluR2 activation is only loosely coupled to release site location, while mGluR7 activation is limited, even when placed in immediate proximity to the release site. These two receptor types might thus encode different modes of synaptic activity patterns: mGluR2 responding to lower frequency stimulation patterns, and mGluR7 being activated only during intense, high-frequency synaptic stimulation. It has been suggested that group III mGluRs act as auto-receptors during repetitive stimulations and modulate release probability (Billups et al., 2005; Pinheiro and Mulle, 2008). On the other hand, it has been described that mGluR7 is constitutively active (Dunn et al., 2018; Kammermeier, 2015; Stachniak et al., 2019), and that activity of mGluR7 is regulated by the transsynaptic interaction with ELFN2 at excitatory synapses (Dunn et al., 2019a; Stachniak et al., 2019). Allosteric modulation of mGluR7 by ELFN2 could thus decrease the threshold for receptor activation or increase its basal activity. Moreover, in our model we assumed a homogenous distribution of G-proteins inside the presynaptic bouton. However, we cannot exclude the possibility that at the active zone there is a higher local concentration of Gα, or that mGluR7 has a higher affinity for G-proteins than mGluR2. Thus, activation of mGluR7 could result in stronger activation of downstream signaling pathway and larger effect on synaptic transmission. Nevertheless, the results from our computational model indicate that mGluR7 positioning relative to the release site is a critical factor increasing the probability of receptor activation.

The spatial segregation of mGluRs in presynaptic boutons could also be a mechanism to compartmentalize the downstream effectors of these receptors. Both mGluR2 and mGluR7 couple to inhibitory $G\alpha_i$ proteins that repress adenylyl cyclase activity, decreasing cAMP production. Indeed, these receptors have overlapping downstream signaling proteins such as PKA and PKC, and are both described to modulate calcium channel activity (de Jong and Verhage, 2009; Ferrero et al., 2013; Martín et al., 2007; Robbe et al., 2002). But, mGluR7 has also been suggested to interact with several other components of the active zone, such as RIM1a (Pelkey et al., 2008), and Munc-13 (Martín et al., 2010). The selective effects of these receptors might thus be explained by their segregated distribution. One of the principal mechanisms of synaptic depression that is shared by these receptors, involves the interaction between the membrane-anchored βγ subunits of the G-protein with voltage-gated $Ca^{2+}$ channels (VGCC) (Kammermeier, 2015; Niswender and Conn, 2010). An important rate-limiting factor in this mechanism is probably the distance between the $G_{\beta\gamma}$ subunits and VGCCs. It could thus be envisioned that the effect of mGluR2 activation on synaptic transmission would not be instantaneous but would be delayed by the diffusion time of βγ subunits to VGCCs enriched at the active zone. For mGluR7 on the other hand, being immobilized in close proximity to release sites, the inhibition of VGCCs might occur much more instantaneously after receptor activation. Altogether, our data indicate that the specific modulatory effects of presynaptic mGluRs on synaptic transmission are in large part determined by their differential localization relative to the release site and their distinct surface diffusion properties.

Given the distinct distribution and diffusion properties of mGluR2 and mGluR7, we speculated that distinct mechanisms control the surface mobility of these receptors. Both C-terminal regions of mGluR2 and mGluR7 contain PDZ binding motifs, but of different types, mGluR2 contains a class I, and mGluR7 a class II binding motif (Hirbec et al., 2002) indicating specific intracellular interaction for each of presynaptic mGluRs. Our data indeed suggest that intracellular interactions mediated by the C-terminal region of mGluR2 regulate receptor diffusion. However, little is known about mGluR2 C-tail-mediated interactions and molecular mechanisms engaged in controlling mGluR2 diffusion remain to be elucidated. Also for mGluR7 it has been suggested that stable surface expression and clustering in presynaptic boutons is controlled by the intracellular interaction with the PDZ-domain containing scaffold protein PICK1 (Boudin et al., 2000; Suh et al., 2008). In contrast, another study showed that the synaptic distribution of an mGluR7 mutant lacking the PDZ binding motif was unaltered (Zhang et al., 2008). Our findings that the intracellular domain of mGluR7 does not contribute to receptor clustering and immobilization at presynaptic boutons are consistent with this, further suggesting that interactions with PICK1 could be important for mGluR7 function but do not instruct receptor localization. Rather, we found an unexpected role of the extracellular domain of mGluR7 in its immobilization at presynaptic plasma membrane. Chimeric mGluR7 variants with substituted ECDs displayed higher diffusion coefficients than wild-type mGluR7 and surface diffusion was no longer restricted to the presynaptic bouton but was virtually unrestricted along the axon. Our data thus suggest that extracellular interactions can efficiently cluster the receptor and that the extracellular domain of mGluR7 is essential for immobilizing and concentrating the receptor at active zones.

The dramatic effect of replacing the extracellular domain of mGluR7 on localization and diffusion suggests that transsynaptic interactions effectively concentrate mGluR7 at synaptic sites. This is strikingly consistent with the emerging notion that transcellular interactions greatly impact GPCR biology (Dunn et al., 2019a). Specifically for group III mGluRs, interactions with the adhesion molecules ELFN1 and ELFN2 have been found to modulate the functional properties of these receptors and potently impact synaptic function (Dunn et al., 2019b, 2018; Sylwestrak and Ghosh, 2012; Tomioka et al., 2014). Here, we provide direct evidence that in hippocampal neurons ELFN2 is present in the PSD, adjacent to the presynaptic active zone where mGluR7 is located. Our experiments further showed that ELFN2 can efficiently recruit mGluR7 to intercellular boundaries and that this recruitment is mediated by the ECD of mGluR7. Together with the pronounced role of the mGluR7 ECD in immobilizing the receptor at synaptic sites, we propose that mGluR7 is concentrated at the active zone by transsynaptic interactions with ELFN2. This specific interaction might then also explain the targeting and clustering of mGluR7 to specific subsets of synapses (Shigemoto et al., 1996). Collectively, the transsynaptic interaction with ELFN2 thus seems to be critical for anchoring mGluR7 at specific synaptic sites while simultaneously regulating receptor activity via allosteric modulation.

Previous studies have suggested that ligand-induced GPCR activation, alters their surface diffusion and oligomerization properties (Calebiro et al., 2013; Kasai and Kusumi, 2014; Sungkaworn et al., 2017; Yanagawa et al., 2018). In heterologous cells the diffusion rate of many GPCRs, including mGluR3 for instance, are significantly reduced after agonist stimulation (Yanagawa et al., 2018). Surprisingly, our data in neurons indicate that the surface mobility of mGluRs is not altered by agonist-induced receptor activation, or acute changes in neuronal activity. Diffusion in the plasma membrane of heterologous cells is likely influenced by other factors than in neuronal membranes. Most notably, the unique membrane composition and expression of cell-type specific interaction partners in neurons are likely to differentially tune the diffusional properties of individual receptors. Indeed, the mobility of the CB1R in the axon decreases after desensitization (Mikasova et al., 2008), while the mobility of another GPCR, MOR does not change after agonist stimulation (Jullié et al., 2020). Our data indicate that for the presynaptic mGluRs, mGluR2 and mGluR7, structural factors, such as interactions with intra- and extracellular components predominantly instruct receptor localization, and that these mechanisms act independently of the receptor activation status. This has potentially important implications for the contribution of these receptors to the regulation of synaptic transmission. mGluR7 is likely to exert its effects very locally, restricted to individual synapses. For mGluR2 on the other hand, it could be speculated that the unchanged, high surface mobility of mGluR2 after activation allows the receptor to activate downstream effectors over larger areas, as has been suggested for the opioid receptor (Jullié et al., 2020). This would imply that, once activated, mGluR2 could spread its effects to neighboring synapses and dampen transmission much more globally than mGluR7 does. We can of course not exclude that only a small, undetectable subpopulation of activated mGluRs is immobilized at specific locations, but given that the threshold for mGluR2 activation is relatively low, it seems likely that the effects of mGluR2 activation are much more widespread than mGluR7. This could also imply that activity of mGluR2 not only modulates synaptic transmission, but perhaps also controls other axonal processes such as protein synthesis, cargo trafficking, or cytoskeleton reorganization.

In conclusion, we identified novel regulatory mechanisms that differentially control the spatial distribution and dynamics of presynaptic glutamate receptors, that have important implications for how these receptors can contribute to the modulation of synaptic transmission. The co-existence of various other and distinct receptor types at presynaptic sites likely provides flexibility and allows synapses to differentially respond to incoming stimulation patterns. Defining the molecular mechanisms that control the dynamic spatial distribution of these receptors will be important to further our understanding of synaptic modulation.

## MATERIALS AND METHODS

### Animals

All experiments required animals were approved by the Dutch Animal Experiments Committee (Dier Experimenten Commissie [DEC]). All animals were treated in accordance with the regulations and guidelines of Utrecht University, and conducted in agreement with Dutch law (Wet op de Dierproeven, 1996) and European regulations (Directive 2010/63/EU).

### Antibodies and reagents

In this study the following primary antibodies were used: mouse anti-Bassoon (1:500 dilution, Enzo, #ADI-VAM-PS003-F, RRID AB_10618753); rabbit anti-ELFN2 (1:100 dilution, Atlas Antibody, #HPA000781, RRID AB_1079280); rabbit anti-GFP (1:2000 dilution, MBL Sanbio, #598, RRID AB_591819); rat anti-HA (1:400 dilution, Sigma, #11867423001, RRID AB_390919); rabbit anti-mGluR2/3 (1:50 dilution, EMD Millipore, #AB1553, RRID AB_90767); rabbit anti-mGluR7 (1:100 dilution, Merck Millipore, #07-239, RRID AB_310459); mouse anti-PSD95 (1:400 dilution, Neuromab, #75– 028, RRID AB_2307331) and anti-GFP nanobodies conjugated with ATTO647N (1:15000 dilution, GFPBooster-ATTO647N, Chromotek, #gba647n). The following secondary antibodies were used: goat Abberior STAR580-conjugated anti-rabbit (1:200 dilution, Abberior GmbH, #2-0012-005-8); goat Abberior STAR635P-conjugated anti-mouse (1:200 dilution, Abberior GmBH, #2-0002-007-5) and goat Alexa Fluor594-conjugated anti-rat (1:200 dilution, Life Technologies, #A-11007). The following chemical reagents were used: 4-aminopyridine (4-AP, TOCRIS, #940), DL-TBOA (TOCRIS, #1223), L-AP4 (TOCRIS, #0103), and LY379268 (TOCRIS, #2453).

**DNA plasmids**

The SEP-mGluR2, ELFN2-GFP and ELFN2-2xHA CRISPR/Cas9 knock-in constructs were designed as described in (Willems et al., 2020). SEP tag was inserted into exon 2 of *Grm2* gene using following target sequence: 5'-AGGGTCAGCACCTTCTTGGC-3'. GFP tag or 2xHA tag were inserted into exon 2 of *Elfn2* gene using following target sequence: 5'- AGACCCCCTTCCAGTAATCA-3'. Plasmids pRK5-mGluR2-GFP and pRK5-myc-mGluR7a (gift from Dr. J. Perroy) were used as PCR template to generate pRK5-SEP-mGluR2 and pRK5-SEP-mGluR7. pRK5-mOrange-mGluR2 and pRK5-mOrange-mGluR7 were created by exchanging SEP with mOrange in pRK5-SEP-mGluR2 and pRK5-SEP-mGluR7. pRK5-SEP-mGluR7-N74K was cloned using a site-directed mutagenesis using the following primers: forward: 5'-GGCGACATCAAGAGGGAGAAAGGGATCCACAGGCTGGAAGC-3' and reverse: 5'-GCTTCCAGCCTGTGGATCCCTTTCTCCCTCTTGATGTCGCC-3'. To create SEP-tagged chimeric variants of mGluR2 and mGluR7, sequences of wild-type receptors in pRK5-SEP-mGluR2 and pRK5-SEP-mGluR7 were replaced by the sequence of the chimeric receptor. Chimeric receptors were cloned by fusing sequences encoding different domains of mGluR2, mGluR7 and mGluR1 as follow:

mGluR2-ICD7: 1-819 aa mGluR2 + 849-913 aa mGluR7;
mGluR2-TMD7: 1-556 aa mGluR2 + 578-848 aa mGluR7 + 820-872 mGluR2;
mGluR2-ECD7: 1-583 aa mGluR7 + 562-872 aa mGluR2;
mGluR7-ICD2: 1-848 aa mGluR7 + 820-872 aa mGluR2;
mGluR7-TMD1: 1-588 aa mGluR7 + 591-839 aa mGluR1+ 849-914 aa mGluR7;
mGluR7-TMD2: 1-588 aa mGluR7 + 568-819 aa mGluR2 + 849-914 aa mGluR7;
mGluR7-ECD1: 1-585 aa mGluR1 + 584-913 aa mGluR7;
mGluR7-ECD2: 1-556 aa mGluR2 + 584-913 aa mGluR7.

Aminoacid numbering is based on sequences in UniPortKB database (mGluR1 - Q13255-1, mGluR2 - P31421-1, mGluR7 - P35400-1) and starts with first aminoacid of signal peptide. pRK5-SEP-mGluR1 (Scheefhals et al., 2019) was used as PCR template for transmembrane and extracellular domain of mGluR1. All chimeric mGluR variants were cloned using Gibson assembly (NEBuilder HiFi DNA assembly cloning kit). pRK5-mOrange-mGluR2-ECD7 was generated by replacing SEP tag in pRK5-SEP-mGluR2-ECD7. Synaptophysin1-mCherry plasmid was generated by replacing pHluorin-tag in Synaptophysin1-pHluorin (gift from L. Lagnado, Addgene plasmid # 24478) with mCherry from pmCherry-N1 (Invitrogen). ELFN2-GFP plasmid was a gift from Dr. E. Sylwestrak (Sylwestrak and Ghosh, 2012). All sequences were verified by DNA sequencing.

**Primary rat neuronal culture and transfection**

Dissociated hippocampal cultures from embryonic day 18 (E18) Wistar rat (Janvier Labs) brains of both genders were prepared as described previously (Cunha-Ferreira et al., 2018). Neurons were plated on 18-mm glass coverslips coated with poly-L-lysine (37.5 mg/ml, Sigma-Aldrich) and laminin (1.25 mg/ml, Roche Diagnostics) at a density of 100,000 neurons per well in 12-well plate. Neurons were growing in Neurobasal Medium (NB; Gibco) supplemented with 2% B27 (Gibco), 0.5 mM L-glutamine (Gibco), 15.6 μM L- glutamic acid (Sigma) and 1% penicillin/streptomycin (Gibco). Once per week, starting from DIV1, half of the medium was refreshed with BrainPhys neuronal medium (BP, STEMCELL Technologies) supplemented with 2% NeuroCult SM1 supplement (STEMCELL Technologies) and 1% penicillin/streptomycin (Gibco). Neurons were transfected at DIV3-4 (knock-in constructs) or DIV10-11 (overexpression constructs) using Lipofectamine 2000 reagent (Invitrogen). Shortly before transfection, neurons were transferred to a plate with fresh NB medium with supplements. Next, a mixture of 2 μg of DNA and 3.3 μl of Lipofectamine in 200 μl of NB medium was incubated for 15 - 30 min and added to each well. After 1 - 2 h, neurons were briefly washed with NB medium and transferred back to the plate with conditioned medium. All experiments were performed using neurons at DIV21-24.

**U2OS cells co-culture assays**

U2OS cells (ATCC HTB-96) were cultured in DMEM (Lonza) supplemented with 10% fetal calf serum (Sigma), 2 mM glutamine and 1% penicillin/streptomycin (Gibco). The day before transfection U2OS cells were seeded in a 6-well plate. Next, cells were transfected using 6 µg of polyethylenimine (PEI, Polysciences) and 4 µg of DNA per well. Cells were transfected either with ELFN2-GFP or mOrange-tagged mGluR2/7. 24 h after transfection, cells were trypsinized, and ELFN2-GFP transfected cells were mixed with mOrange-mGluR2/7 transfected cells in a 1:1 ratio and seeded on 18-mm glass coverslips. 48 h after trypsinization, U2OS cells were fixed with 4% PFA for 10 min at RT, washed three times with PBS and mounted in Mowiol mounting medium (Sigma). Imaging of U2OS cells was performed with Zeiss LSM 700 confocal microscope using 63× NA 1.40 oil objective.

**Immunostaining and gSTED imaging**

Neurons at DIV21 were fixed with 4% PFA and 4% sucrose in PBS for 10 min at RT and washed three times with PBS supplemented with 100 mM glycine. Next, cells were permeabilized and blocked with 0.1% Triton-X, 10% normal goat serum and 100 mM glycine in PBS for 1 h at 37°C. Neurons were incubated with primary antibodies diluted in PBS supplemented with 0.1% Triton-X, 5% normal goat serum and 100 mM glycine for 3 - 4 h at RT. After three times washing cells with PBS with 100 mM glycine, neurons were incubated with secondary antibodies diluted in PBS supplements with 0.1% Triton-X, 5% normal goat serum and 100 mM glycine for 1 h at RT. Cell were washed two times with PBS with 100 mM glycine and two times with PBS. Neurons were mounted in Mowiol mounting medium (Sigma). Dual-color gated STED imaging was performed with a Leica TCS SP8 STED 3 microscope using a HC PL APO 100/1.4 oil-immersion STED WHITE objective. Abberior STAR 580 and 635P were excited with 561 nm and 633 nm pulsed laser light (white light laser, 80 MHz) respectively. Both Abberior STAR 580 and 635P were depleted with a 775 nm pulsed depletion laser. Fluorescence emission was detected using Leica HyD hybrid detector with gating time from 0.5 ns to 6 ns.

**Live-cell imaging and fluorescence recovery after photobleaching (FRAP) experiments**

For all live-cell imaging experiments, cells were kept in a modified Tyrode's solution (pH 7.4) containing 25 mM HEPES, 119 mM NaCl, 2.4 mM KCl, 2 mM $CaCl_2$, 2 mM $MgCl_2$, 30 mM glucose. FRAP experiments were carried out in an environmental chamber at 37$^{o}$C (TokaHit) on an inverted Nikon Ti Eclipse microscope equipped with a confocal spinning disk unit (Yokogawa), an ILas FRAP unit (Roper Scientific France/ PICT-IBiSA, Institut Curie), and 491-nm laser (Cobolt Calypso). Fluorescence emission was detected using a 100x oil-immersion objective (Nikon Apo, NA 1.4) together with an EM-CCD camera (Photometirc Evolve 512) controlled by MetaMorph7.7 software (Molecular Divices). Images were acquired at 1 Hz with an exposure time between 100 and 200 ms. 3 - 5 ROIs covering single boutons were bleached per field of view.

**Single-molecule tracking with uPAINT**

Single molecule tracking was carried out in modified Tyrode's solution supplement with 0.8% BSA and ATTO647N-conjugated anti-GFP nanobodies (imaging solution) on Nanoimager microscope (Oxford Nanoimaging; ONI) equipped with a 100x oil-immersion objective (Olympus Plans Apo, NA 1.4), an XYZ closed-loop piezo stage, 471-nm, 561-nm and 640-

nm lasers used for excitation of SEP, mCherry and ATTO647N respectively. Fluorescence emission was detected using a sCMOS camera (ORCA Flash 4, Hamamatsu). 3,000 images were acquired in stream mode at 50 Hz in TIRF. Before every tracking acquisition, 30 frames of SEP and mCherry signal were taken to visualize cell morphology or boutons. To determined how activity of receptors influences their diffusion, first control acquisitions (2 - 3 fields of view per coverslip) were taken, next chemical reagents or high $K^+$ solution (2x) were added to imaging chamber, incubated for 3 - 5 min and final acquisitions of previously imaged fields of views were performed. High $K^+$ solution was prepared by replacing 45 mM NaCl with KCl. Total incubation times with chemical reagents or high $K^+$ solution did not exceed 15 min.

**Computational modeling of mGluR activity**

***Receptor model:*** To study the time-dependent response of mGluRs upon glutamate release, a G-protein-coupled receptor model was combined with the time-dependent concentration profile of glutamate released from synaptic vesicles. The cubic ternary complex activation model (cTCAM) of GPCR signaling describes the interaction of the receptors $R$, ligands $L$ and G-proteins $G$ (Kinzer-Ursem and Linderman, 2007). The receptors can complex with G-proteins to form $RG$ and furthermore, can be in an active state $R^*$ denoted by the asterisk. G proteins are produced by a cascade of $G\alpha_{GTP}$ hydrolysis and $G_{\beta\gamma}$ binding. The reactions are described by the following differential equations:

$$\frac{dR}{dt} = -(k_1 + k_3 L + \eta k_{11} G)R + \left(\frac{k_1}{K_{act}}\right)R^* + \left(\frac{\eta k_{11}}{K_g}\right)RG + \left(\frac{k_3}{K_a}\right)LR$$

$$\frac{dLR}{dt} = -\left(\frac{k_3}{K_a} + \alpha k_a + \eta k_{11} G\right)LR + (k_3 L)R + \left(\frac{k_1}{K_{act}}\right)LR^* + \left(\frac{\eta k_{11}}{\gamma K_g}\right)LRG$$

$$\frac{dRG}{dt} = (\eta k_{11} G)R - \left(\frac{\eta k_{11}}{K_g} + k_3 L + \beta k_1\right)RG + \left(\frac{k_3}{\gamma K_a}\right)LRG + \left(\frac{k_1}{K_{act}}\right)R^*G$$

$$\frac{dLRG}{dt} = (k_3 L)RG - \left(\frac{k_3}{\gamma K_a} + \frac{\eta k_{11}}{\gamma K_g} + \alpha\beta\delta K_1\right)LRG + (\eta k_{11} G)LR + \left(\frac{k_1}{K_{act}}\right)LR^*G$$

$$\frac{dR^*}{dt} = k_1 R - \left(\frac{k_1}{K_{act}} + \alpha k_3 L + \beta k_{11} G\right)R^* + \left(\frac{k_3}{K_a}\right)LR^* + \left(\frac{k_{11}}{K_g}\right)R^*G + k_{Gact}R^*G$$

$$\frac{dLR^*}{dt} = \alpha k_1 LR - \left(\frac{k_1}{K_{act}} + \frac{k_3}{K_a} + \beta k_{11} G\right)LR^* + (\alpha k_3 L)R^* + \left(\frac{k_{11}}{\delta\gamma K_g}\right)LR^*G + k_{Gact}LR^*G$$

$$\frac{dR^*G}{dt} = (\beta k_{11} G)R^* - \left(\frac{k_{11}}{K_g} + \frac{k_1}{K_{act}} + \alpha k_3 L + k_{Gact}\right)R^*G + \beta k_1 RG + \left(\frac{k_3}{\delta\gamma K_a}\right)LR^*G$$

$$\frac{dLR^*G}{dt} = (\alpha k_3 L)R^*G - \left(\frac{k_3}{\delta\gamma K_a} + \frac{k_{11}}{\delta\gamma K_g} + \frac{k_1}{K_{act}} + k_{Gact}\right)LR^*G + (\beta k_{11} G)LR^* + \alpha\beta\delta k_1 LRG$$

$$\frac{dG\alpha_{GTP}}{dt} = k_{Gact}(R^*G + LR^*G) - k_{GTP}G\alpha_{GTP}$$

$$\frac{dG\alpha_{GDP}}{dt} = k_{Gact}G\alpha_{GTP} - (k_G G_{\beta\gamma})G\alpha_{GDP}$$

$$\frac{dG_{\beta\gamma}}{dt} = k_{Gact}(R^*G + LR^*G) - (k_G G\alpha_{GDP})G_{\beta\gamma}$$

$$\frac{dG}{dt} = -(\eta k_{11} R + \eta k_{11} LR + \beta k_{11} LR^* + \beta k_{11} R^*)G + \left(\frac{\eta k_{11}}{K_g}\right)RG + \left(\frac{\eta k_{11}}{\gamma K_g}\right)LRG$$

$$+ \left(\frac{k_{11}}{\delta\gamma K_g}\right)LR^*G + \left(\frac{k_{11}}{K_g}\right)R^*G + (k_G G\alpha_{GDP})G_{\beta\gamma}$$

To find the steady-state solution without ligand ($L = 0$), these equations were solved with initial conditions $R = 100$, $G = 1000$ and the remaining variables set to zero using the NDSolve function of Mathematica (version 12.0, Wolfram Research Inc.). The numerical values for the used parameters have been described previously (Kinzer-Ursem and Linderman, 2007) and are summarized in Table S1. The number of receptors and G-proteins in presynaptic bouton are estimated based on quantitative mass-spectrometry data published in (Wilhelm et al., 2014). To describe the different behaviors of mGluR2 and mGluR7, only the association constant $K_a$ was adjusted to match previously published $EC_{50}$ values: 10 µM for mGluR2 and 1 mM for mGluR7 (Schoepp et al., 1999). The $EC_{50}$ value is the concentration of the ligand that gives the half maximum response. Hence, the response was estimated by the number of $G\alpha_{GTP}$. The steady-state solution without ligand was used as the initial state of the system and the new steady-state values for different amounts of the ligand were numerically determined. The relative normalized change of $G\alpha_{GTP}$ gives the response:

$$\frac{G\alpha_{GTP}(L) - G\alpha_{GTP}(L=0)}{G\alpha_{GTP}(L \gg 0) - G\alpha_{GTP}(L=0)}$$

To obtain the EC$_{50}$ value, the following function was fitted to the data points from the numerical solution (Figure 6D):

$$\frac{1}{1+\left(\frac{EC_{50}}{L}\right)^n}$$

In this way, a parameterization of mGluR2 with $K_a = 0.7\cdot10^4$ M$^{-1}$ and respective EC$_{50}$ = 10 µM, and mGluR7 with $K_a$ = 60 M$^{-1}$ and respective EC$_{50}$ = 1.15 mM was obtained. To investigate the ligand receptor affinity, the normalized response of the sum of all formed receptor - ligand complexes was determined as (Figure 6C):

$$\frac{LR(L) + LRG(L) + LR^*(L) + LR^*G(L)}{LR(L \gg 1) + LRG(L \gg 1) + LR^*(L \gg 1) + LR^*G(L \gg 1)}$$

***Diffusion model:*** The time-dependent concentration of glutamate released from a synaptic vesicle was described as a point source on an infinite plane. The solution of the diffusion equation gives the surface density:

$$c(r,t) = \frac{N}{4\pi Dt}\exp\left(\frac{-r^2}{4Dt}\right)$$

in which $r$: the distance from the source,

$N = 3000$ : the total amount of glutamate released,

$D = 4\cdot10^{-9}\frac{m^2}{s}$: the diffusion constant of glutamate (Kessler, 2013).

To transform the surface density into a concentration the following formula was used:

$$N = \frac{4}{3}\pi r_v^3 C_0$$

in which $r_v = 25\ nm$: the radius of a vesicle,

$C_0$: the glutamate concentration inside the vesicle.

Next, the surface density was divided by the $d = 20\ nm$ width of the synaptic cleft to obtain:

$$C(r,t) = \frac{r_v^3 C_0}{3dDt} \exp\left(\frac{-r^2}{4Dt}\right)$$

Hence, the initial concentration is given by:

$$C_0 = \frac{N}{N_A \frac{4}{3}\pi r_v^3 10^3} = 75\ mM$$

in which $N_A$: Avogadros's constant.

To describe the glutamate concentration from a sequence of vesicles release events, superposition was used as follows:

$$L(t) = \sum_{i=0}^{n-1} H\left(t - \frac{i}{f}\right) C\left(r, t - \frac{i}{f}\right)$$

in which $n$: the number of vesicles released,

$f$: the release frequency,

$H(x) = \begin{cases} 1 & x > 0 \\ 0 & otherwise \end{cases}$ : a step function.

The diffusion profile was combined with the receptor model and the differential equations were solved numerically for a given distance $r$ from the release site. For the initial conditions, the steady-state solution without ligand was used. Because of the non-linearities in the equations and the possible large values of the concentration profile for small times, to solve the equations numerically, we reduced the accuracy and precision of the numerical integration method in Mathematica's NDSolve function. This adjustment potentially introduced an error of less than 5 percent, which is small enough to be neglected in our analysis and conclusions.

**Table supplement 1.** Parameters used in cTCAM model of presynaptic mGluRs activity

| Parameter [1] | Symbol | Value (unit) |
|---|---|---|
| Receptor activation rate | $k_1$ | $0.1\ s^{-1}$ |
| #active/#inactive receptors | $K_{act}$ | 0.01 |
| Receptors - G protein collision efficiency | $\eta$ | 0.5 |
| Receptor - G protein association rate | $k_{11}$ | $1 \cdot 10^{-4}$ #/cell $s^{-1}$ |
| Receptor - G protein binding affinity | $K_g$ | $1 \cdot 10^{-4}$ #/cell |
| Ligand - Receptor association constant | $k_3$ | $1 \cdot 10^{7}\ M^{-1}\ s^{-1}$ |
| Ligand - Receptor equilibrium association constant for mGluR2 [2] | $K_a$ | $0.7 \cdot 10^{4}\ M^{-1}$ |
| Ligand - Receptor equilibrium association constant for mGluR7 [2] | $K_a$ | $60\ M^{-1}$ |
| Parameter for receptor activation via ligand binding | $\alpha$ | 5 |
| Parameter for G protein coupling via receptor activation | $\beta$ | 5 |
| Joint coupling parameter (activation, ligand binding, G protein coupling) | $\delta$ | 5 |
| Parameter for G protein coupling via ligand binding | $\gamma$ | 5 |
| G protein activation rate | $k_{Gact}$ | $5\ s^{-1}$ |
| GTP hydrolysis rate | $k_{GTP}$ | $1\ s^{-1}$ |
| $G_{\alpha\beta\gamma}$ association constant | $k_G$ | $1 \cdot 10^{-4}$ #/cell $s^{-1}$ |
| Total numbers of receptors [3] | $R_{tot}$ | 100 |
| Total numbers of G proteins [3] | $G_{tot}$ | 1000 |

[1] values used in simulation are taken from (Kinzer-Ursem and Linderman, 2007) unless indicated otherwise
[2] $K_a$ for mGluR2 and mGluR7 was estimated by calibration cTCAM model to match output $G_{\alpha GTP}$ concentration with published $EC_{50}$ values (Schoepp et al., 1999).
[3] total numbers of presynaptic mGluRs and G-proteins inside presynaptic boutons were estimated based on quantitative mass-spectrometry data published in (Wilhelm et al., 2014).

**Data analysis**

***Quantification of co-localization:*** Analysis of co-localization between Bsn and mGluRs was done using Spot Detector and Colocalization Studio plug-ins built-in in Icy software (De Chaumont et al., 2012). Objects detected with Spot Detector (size of detected spots: ~7 pixel with sensitivity 100 and ~13 pixels with sensitivity 80) were loaded into Colocalization Studio and statistical object distance analysis (SODA) (Lagache et al., 2018) was performed to obtain the fraction of mGluR spots co-localized with Bsn spots.

***Quantification of bouton enrichment of overexpressed SEP-mGluRs:*** Neuron co-expressing cytosolic mCherry and SEP-mGluR2 or SEP-mGluR7 were fixed at DIV21 with 4% PFA and 4% sucrose from 10 min in RT. Next, cells were washed three times with PBS and mounted in Mowiol mounting medium (Sigma). Imaging was performed on with Zeiss LSM 700 confocal microscope using 63× NA 1.40 oil objective. To analyze enrichment of mGluRs in presynaptic boutons, line profiles along boutons and neighboring axonal region were drawn in ImageJ (line width 3 pixels). Next, intensity profiles were fitted with a Gaussian function in GraphPad Prism. To calculate the ratio of intensity in bouton over axon, the amplitude of the Gaussian fit was divided by the minimum value of the fit.

***Quantification of FRAP experiments:*** Time series obtained during FRAP experiments were corrected for drift when needed using Template Matching plug-in in ImageJ. Circular ROIs with the size of the bleached area were drawn in ImageJ. Fluorescent intensity transients were normalized by subtracting the intensity values of the $1^{st}$ frame after bleaching and dividing by the average intensity value of the baseline (5 frames before bleaching). Mobile fraction was calculated by averaging the values of the last 5 points of fluorescent transients. Half-time of recovery was determined by fitting a single exponential function to the recovery traces.

***Single-molecule tracking analysis:*** NimOS software (Oxford Nanoimager; ONI) was used to detect localization of single molecules in uPAINT experiments. Molecules with a localization precision < 50 nm and photon count > 200 photons were used for analysis. To filter out unspecific background localizations from outside neurons, a cell mask based on the SEP image was created using an adaptive image threshold in Matlab (sensitivity 40-55). Only localizations inside the mask were included in further analysis. Tracking and calculation of the diffusion coefficient were performed in custom-written Matlab (MathWorks) scripts described previously (Willems et al., 2020). Only trajectories longer than 30 frames were used to estimate the instantaneous diffusion coefficient. Classification of molecule state as mobile or immobile was based on ratio between the radius of gyration and mean step size of individual trajectories using formula $\frac{\sqrt{\pi/2} \times radius\ of\ gyration}{mean\ step\ size}$ (Golan and Sherman, 2017). Molecules with a ratio < 2.11 were considered immobile. Mask of presynaptic boutons was created based on the TIRF image of Synaptophysin1-mCherry as previously described(Li and Blanpied, 2016). Synaptic trajectories were defined as trajectories which had at least one localization inside bouton mask.

***Statistical analysis:*** All used in this study statistical tests are described in figure legends and the main text. All statistical analysis and graphs were prepared in GraphPad Prism.

## AUTHOR CONTRIBUTIONS

Conceptualization, Methodology, Validation, & Formal Analysis, A.B., F.B. and H.D.M.; Investigation, A.B. and F.B.; Resources, H.D.M.; Writing – Original Draft & Editing, A.B. and H.D.M.; Writing – Review, F.B.; Visualization, A.B.; Supervision, H.D.M.; Funding Acquisition, H.D.M.


## ACKNOWLEDGEMENTS

We would like to thank dr. Arthur de Jong for critical reading of the manuscript, Manon Westra for help with Matlab scripts and all members of the MacGillavry lab for helpful discussions. This work was supported by the European Research Council (ERC-StG 716011) to H.D.M.


## DECLARATION OF INTERESTS

The authors declare no competing interests.

## REFERENCES

Billups B, Graham BP, Wong AYC, Forsythe ID. 2005. Unmasking group III metabotropic glutamate autoreceptor function at excitatory synapses in the rat CNS. *J Physiol* **565**:885–896. doi:10.1113/jphysiol.2005.086736

Boudin H, Doan A, Xia J, Shigemoto R, Huganir RL, Worley P, Craig AM. 2000. Presynaptic clustering of mGluR7a requires the PICK1PDZ domain binding site. *Neuron* **28**:485–497.

Bushell TJ, Sansig G, Collett VJ, van der Putten H, Collingridge GL. 2002. Altered short-term synaptic plasticity in mice lacking the metabotropic glutamate receptor mGlu7. *ScientificWorldJournal* **2**:730–7. doi:10.1100/tsw.2002.146

Calebiro D, Rieken F, Wagner J, Sungkaworn T, Zabel U, Borzi A, Cocucci E, Zürn A, Lohse MJ. 2013. Single-molecule analysis of fluorescently labeled G-protein-coupled receptors reveals complexes with distinct dynamics and organization. *Proc Natl Acad Sci U S A* **110**:743–748. doi:10.1073/pnas.1205798110

Cunha-Ferreira I, Chazeau A, Buijs RR, Stucchi R, Will L, Pan X, Adolfs Y, van der Meer C, Wolthuis JC, Kahn OI, Schätzle P, Altelaar M, Pasterkamp RJ, Kapitein LC, Hoogenraad CC. 2018. The HAUS Complex Is a Key Regulator of Non-centrosomal Microtubule Organization during Neuronal Development. *Cell Rep* **24**:791–800. doi:10.1016/j.celrep.2018.06.093

Dasgupta A, Lim YJ, Kumar K, Baby N, Pang KLK, Benoy A, Behnisch T, Sajikumar S. 2020. Group III metabotropic glutamate receptors gate long-term potentiation and synaptic tagging/capture in rat hippocampal area CA2. *Elife* **9**:1–20. doi:10.7554/elife.55344

De Chaumont F, Dallongeville S, Chenouard N, Hervé N, Pop S, Provoost T, Meas-Yedid V, Pankajakshan P, Lecomte T, Le Montagner Y, Lagache T, Dufour A, Olivo-Marin JC. 2012. Icy: An open bioimage informatics platform for extended reproducible research. *Nat Methods* **9**:690–696. doi:10.1038/nmeth.2075

de Jong AP, Verhage M. 2009. Presynaptic signal transduction pathways that modulate synaptic transmission. *Curr Opin Neurobiol* **19**:245–253. doi:10.1016/j.conb.2009.06.005

Diamond JS, Jahr CE. 1997. Transporters buffer synaptically released glutamate on a submillisecond time scale. *J Neurosci* **17**:4672–4687. doi:10.1523/jneurosci.17-12-04672.1997

Dunn HA, Orlandi C, Martemyanov KA. 2019a. Beyond the ligand: Extracellular and transcellular G protein-coupled receptor complexes in physiology and pharmacology. *Pharmacol Rev* **71**:503–519. doi:10.1124/pr.119.018044

Dunn HA, Patil DN, Cao Y, Orlandi C, Martemyanov KA. 2018. Synaptic adhesion protein ELFN1 is a selective allosteric modulator of group III metabotropic glutamate receptors in trans. *Proc Natl Acad Sci* **115**:5022–5027. doi:10.1073/pnas.1722498115

Dunn HA, Zucca S, Dao M, Orlandi C, Martemyanov KA. 2019b. ELFN2 is a postsynaptic cell adhesion molecule with essential roles in controlling group III mGluRs in the brain and neuropsychiatric behavior. *Mol Psychiatry* **24**:1902–1919. doi:10.1038/s41380-019-0512-3

Ferrero JJ, Bartolomé-Martín D, Torres M, Sánchez-Prieto J. 2013. Potentiation of mGlu7 receptor-mediated glutamate release at nerve terminals containing N and P/Q type Ca2+channels. *Neuropharmacology* **67**:213–222. doi:10.1016/j.neuropharm.2012.10.032

Francesconi A, Duvoisin RM. 2002. Alternative splicing unmasks dendritic and axonal targeting signals in metabotropic glutamate receptor 1. *J Neurosci* **22**:2196–205. doi:10.1523/jneurosci.22-06-02196.2002

Giannone G, Hosy E, Levet F, Constals A, Schulze K, Sobolevsky AI, Rosconi MP, Gouaux E, Tampe R, Choquet D, Cognet L. 2010. Dynamic superresolution imaging of endogenous proteins on living cells at ultra-high density. *Biophys J* **99**:1303–1310. doi:10.1016/j.bpj.2010.06.005

Golan Y, Sherman E. 2017. Resolving mixed mechanisms of protein subdiffusion at the T cell plasma membrane. *Nat Commun* **8**:1–15. doi:10.1038/ncomms15851

Gutzeit VA, Thibado J, Stor DS, Zhou Z, Blanchard SC, Andersen OS, Levitz J. 2019. Conformational dynamics between transmembrane domains and allosteric modulation of a metabotropic glutamate receptor. *Elife* **8**:1–29. doi:10.7554/elife.45116

Hirbec H, Perestenko O, Nishimune A, Meyer G, Nakanishi S, Henley JM, Dev KK. 2002. The PDZ proteins PICK1, GRIP, and syntenin bind multiple glutamate receptor subtypes. Analysis of PDZ binding motifs. *J Biol Chem* **277**:15221–15224. doi:10.1074/jbc.C200112200

Jullié D, Stoeber M, Sibarita JB, Zieger HL, Bartol TM, Arttamangkul S, Sejnowski TJ, Hosy E, von Zastrow M. 2020. A Discrete Presynaptic Vesicle Cycle for Neuromodulator Receptors. *Neuron* **105**:663-677.e8. doi:10.1016/j.neuron.2019.11.016

Kamiya H, Ozawa S. 1999. Dual mechanism for presynaptic modulation by axonal metabotropic glutamate receptor at the mouse mossy fibre-CAS synapse. *J Physiol* **518**:497–506. doi:10.1111/j.1469-7793.1999.0497p.x

Kammermeier PJ. 2015. Constitutive activity of metabotropic glutamate receptor 7. *BMC Neurosci* **16**:17. doi:10.1186/s12868-015-0154-6

Kang HJ, Wilkins AD, Lichtarge O, Wensel TG. 2015. Determinants of endogenous ligand specificity divergence among metabotropic glutamate receptors. *J Biol Chem* **290**:2870–2878. doi:10.1074/jbc.M114.622233

Kasai RS, Kusumi A. 2014. Single-molecule imaging revealed dynamic GPCR dimerization. *Curr Opin Cell Biol* **27**:78–86. doi:10.1016/j.ceb.2013.11.008

Kessler JP. 2013. Control of Cleft Glutamate Concentration and Glutamate Spill-Out by Perisynaptic Glia: Uptake and Diffusion Barriers. *PLoS One* **8**. doi:10.1371/journal.pone.0070791

Kinoshita A, Shigemoto R, Ohishi H, Van Der Putten H, Mizuno N. 1998. Immunohistochemical localization of metabotropic glutamate receptors, mGluR7a and mGluR7b, in the central nervous system of the adult rat and mouse: A light and electron microscopic study. *J Comp Neurol* **393**:332–352. doi:10.1002/(SICI)1096-9861(19980413)393:3<332::AID-CNE6>3.0.CO;2-2

Kinzer-Ursem TL, Linderman JJ. 2007. Both ligand- and cell-specific parameters control ligand agonism in a kinetic model of G protein-coupled receptor signaling. *PLoS Comput Biol* **3**:0084–0094. doi:10.1371/journal.pcbi.0030006

Klar R, Walker AG, Ghose D, Grueter B a, Engers DW, Hopkins CR, Lindsley CW, Xiang Z, Conn PJ, Niswender CM. 2015. Activation of Metabotropic Glutamate Receptor 7 Is Required for Induction of Long-Term Potentiation at SC-CA1 Synapses in the Hippocampus. *J Neurosci* **35**:7600–15. doi:10.1523/JNEUROSCI.4543-14.2015

Lagache T, Grassart A, Dallongeville S, Faklaris O, Sauvonnet N, Dufour A, Danglot L, Olivo-Marin JC. 2018. Mapping molecular assemblies with fluorescence microscopy and object-based spatial statistics. *Nat Commun* **9**:102–108. doi:10.1016/j.ijrobp.2005.11.033

Li TP, Blanpied TA. 2016. Control of transmembrane protein diffusion within the postsynaptic density assessed by simultaneous single-molecule tracking and localization microscopy. *Front Synaptic Neurosci* **8**:1–14. doi:10.3389/fnsyn.2016.00019

Lisman JE, Raghavachari S, Tsien RW. 2007. The sequence of events that underlie quantal transmission at central glutamatergic synapses. *Nat Rev Neurosci* **8**:597–609. doi:10.1038/nrn2191

Martín R, Durroux T, Ciruela F, Torres M, Pin JP, Sánchez-Prieto J. 2010. The metabotropic glutamate receptor mGlu7 activates phospholipase C, translocates munc-13-1 protein, and potentiates glutamate release at cerebrocortical nerve terminals. *J Biol Chem* **285**:17907–17917. doi:10.1074/jbc.M109.080838

Martín R, Ferrero JJ, Collado-Alsina A, Aguado C, Luján R, Torres M, Sánchez-Prieto J. 2018. Bidirectional modulation of glutamatergic synaptic transmission by metabotropic glutamate type 7 receptors at Schaffer collateral–CA1 hippocampal synapses. *J Physiol* **596**:921–940. doi:10.1113/JP275371

Martín R, Torres M, Sánchez-Prieto J. 2007. mGluR7 inhibits glutamate release through a PKC-independent decrease in the activity of P/Q-type Ca2+ channels and by diminishing cAMP in hippocampal nerve terminals. *Eur J Neurosci* **26**:312–22. doi:10.1111/j.1460-9568.2007.05660.x

Mikasova L, Groc L, Choquet D, Manzoni OJ. 2008. Altered surface trafficking of presynaptic cannabinoid type 1 receptor in and out synaptic terminals parallels receptor desensitization. *Proc Natl Acad Sci U S A* **105**:18596–18601. doi:10.1073/pnas.0805959105

Millán C, Luján R, Shigemoto R, Sánchez-Prieto J. 2002. The inhibition of glutamate release by metabotropic glutamate receptor 7 affects both [Ca2+]c and cAMP: evidence for a strong reduction of Ca2+ entry in single nerve terminals. *J Biol Chem* **277**:14092–101. doi:10.1074/jbc.M109044200

Muly EC, Mania I, Guo J-D, Rainnie DG. 2007. Group II metabotropic glutamate receptors in anxiety circuitry: Correspondence of physiological response and subcellular distribution. *J Comp Neurol* **505**:682–700. doi:10.1002/cne.21525

Niswender CM, Conn PJ. 2010. Metabotropic glutamate receptors: physiology, pharmacology, and disease. *Annu Rev Pharmacol Toxicol* **50**:295–322. doi:10.1146/annurev.pharmtox.011008.145533

Ohishi H, Ogawa-Meguro R, Shigemoto R, Kaneko T, Nakanishi S, Mizuno N. 1994. Immunohistochemical localization of metabotropic glutamate receptors, mGluR2 and mGluR3, in rat cerebellar cortex. *Neuron* **13**:55–66. doi:10.1016/0896-6273(94)90459-6

Okamoto N, Hori S, Akazawa C, Hayashi Y, Shigemoto R, Mizuno N, Nakanishi S. 1994. Molecular characterization of a new metabotropic glutamate receptor mGluR7 coupled to inhibitory cyclic AMP signal transduction. *J Biol Chem* **269**:1231–1236.

Pelkey KA, Lavezzari G, Racca C, Roche KW, McBain CJ. 2005. mGluR7 is a metaplastic switch controlling bidirectional plasticity of feedforward inhibition. *Neuron* **46**:89–102. doi:10.1016/j.neuron.2005.02.011

Pelkey KA, Topolnik L, Yuan XQ, Lacaille JC, McBain CJ. 2008. State-Dependent cAMP Sensitivity of Presynaptic Function Underlies Metaplasticity in a Hippocampal Feedforward Inhibitory Circuit. *Neuron* **60**:980–987. doi:10.1016/j.neuron.2008.11.018

Petralia RS, Wang Y-X, Niedzielski AS, Wenthold RJ. 1996. The metabotropic glutamate receptors, MGLUR2 and MGLUR3, show unique postsynaptic, presynaptic and glial localizations. *Neuroscience* **71**:949–976. doi:10.1016/0306-4522(95)00533-1

Pinheiro PS, Mulle C. 2008. Presynaptic glutamate receptors: physiological functions and mechanisms of action.

*Nat Rev Neurosci* **9**:423–436. doi:10.1038/nrn2379

Reiner A, Levitz J. 2018. Glutamatergic Signaling in the Central Nervous System: Ionotropic and Metabotropic Receptors in Concert. *Neuron* **98**:1080–1098. doi:10.1016/j.neuron.2018.05.018

Robbe D, Alonso G, Chaumont S, Bockaert J, Manzoni OJ. 2002. Role of p/q-Ca2+ channels in metabotropic glutamate receptor 2/3-dependent presynaptic long-term depression at nucleus accumbens synapses. *J Neurosci* **22**:4346–4356. doi:20026420\r22/11/4346 [pii]

Sansig G, Bushell TJ, Clarke VR, Rozov A, Burnashev N, Portet C, Gasparini F, Schmutz M, Klebs K, Shigemoto R, Flor PJ, Kuhn R, Knoepfel T, Schroeder M, Hampson DR, Collett VJ, Zhang C, Duvoisin RM, Collingridge GL, van Der Putten H. 2001. Increased seizure susceptibility in mice lacking metabotropic glutamate receptor 7. *J Neurosci* **21**:8734–45.

Scanziani M, Salin PA, Vogt KE, Malenka RC, Nicoll RA. 1997. Use-dependent increases in glutamate concentration activate presynaptic metabotropic glutamate receptors. *Nature* **385**:630–4. doi:10.1038/385630a0

Scheefhals N, Catsburg LAE, Westerveld ML, Blanpied TA, Hoogenraad CC, MacGillavry HD. 2019. Shank Proteins Couple the Endocytic Zone to the Postsynaptic Density to Control Trafficking and Signaling of Metabotropic Glutamate Receptor 5. *Cell Rep* **29**:258-269.e8. doi:10.1016/j.celrep.2019.08.102

Schoepp DD, Jane DE, Monn JA. 1999. Pharmacological agents acting at subtypes of metabotropic glutamate receptors. *Neuropharmacology* **38**:1431–1476. doi:10.1016/S0028-3908(99)00092-1

Shigemoto R, Kinoshita A, Wada E, Nomura S, Ohishi H, Takada M, Flor PJ, Neki A, Abe T, Nakanishi S, Mizuno N. 1997. Differential presynaptic localization of metabotropic glutamate receptor subtypes in the rat hippocampus. *J Neurosci* **17**:7503–22. doi:9295396

Shigemoto R, Kulik A, Roberts JDB, Ohishi H, Nusser Z, Kaneko T, Somogyi P. 1996. Target-cell-specific concentration of a metabotropic glutamate receptor in the presynaptic active zone. *Nature* **381**:523–5. doi:10.1038/381523a0

Siddig S, Aufmkolk S, Doose S, Jobin M-L, Werner C, Sauer M, Calebiro D. 2020. Super-resolution imaging reveals the nanoscale organization of metabotropic glutamate receptors at presynaptic active zones. *Sci Adv* **6**:eaay7193. doi:10.1126/sciadv.aay7193

Stachniak XTJ, Sylwestrak XEL, Scheiffele XP, Hall BJ, Ghosh A, Stachniak TJ, Sylwestrak EL, Scheiffele P, Hall BJ, Ghosh A. 2019. Elfn1-Induced Constitutive Activation of mGluR7 Determines Frequency-Dependent Recruitment of Somatostatin Interneurons. *J Neurosci* **39**:4461–4474.

doi:10.1523/jneurosci.2276-18.2019

Suh YH, Pelkey KA, Lavezzari G, Roche PA, Huganir RL, McBain CJ, Roche KW. 2008. Corequirement of PICK1 Binding and PKC Phosphorylation for Stable Surface Expression of the Metabotropic Glutamate Receptor mGluR7. *Neuron* **58**:736–48. doi:10.1016/j.neuron.2008.03.028

Sungkaworn T, Jobin ML, Burnecki K, Weron A, Lohse MJ, Calebiro D. 2017. Single-molecule imaging reveals receptor-G protein interactions at cell surface hot spots. *Nature* **550**:543–547. doi:10.1038/nature24264

Sylwestrak EL, Ghosh A. 2012. Elfn1 regulates target-specific release probability at CA1-interneuron synapses. *Science (80- )* **338**:536–540. doi:10.1126/science.1222482

Tomioka NH, Yasuda H, Miyamoto H, Hatayama M, Morimura N, Matsumoto Y, Suzuki T, Odagawa M, Odaka YS, Iwayama Y, Won Um J, Ko J, Inoue Y, Kaneko S, Hirose S, Yamada K, Yoshikawa T, Yamakawa K, Aruga J. 2014. Elfn1 recruits presynaptic mGluR7 in trans and its loss results in seizures. *Nat Commun* **5**:1–16. doi:10.1038/ncomms5501

Wilhelm BG, Mandad S, Truckenbrodt S, Kröhnert K, Schäfer C, Rammner B, Koo SJ, Claßen G a, Krauss M, Haucke V, Urlaub H, Rizzoli SO. 2014. Composition of isolated synaptic boutons reveals the amounts of vesicle trafficking proteins. *Science (80- )* **344**:1023–8. doi:10.1126/science.1252884

Willems J, de Jong APH, Scheefhals N, Mertens E, Catsburg LAE, Poorthuis RB, de Winter F, Verhaagen J, Meye FJ, MacGillavry HD. 2020. ORANGE: A CRISPR/Cas9-based genome editing toolbox for epitope tagging of endogenous proteins in neurons. *PLoS Biol* **18**:e3000665. doi:10.1371/journal.pbio.3000665

Woolley ML, Pemberton DJ, Bate S, Corti C, Jones DNC. 2008. The mGlu2 but not the mGlu3 receptor mediates the actions of the mGluR2/3 agonist, LY379268, in mouse models predictive of antipsychotic activity. *Psychopharmacology (Berl)* **196**:431–440. doi:10.1007/s00213-007-0974-x

Yanagawa M, Hiroshima M, Togashi Y, Abe M, Yamashita T, Shichida Y, Murata M, Ueda M, Sako Y. 2018. Single-molecule diffusion-based estimation of ligand effects on G protein-coupled receptors. *Sci Signal* **11**. doi:10.1126/scisignal.aao1917

Zhang C-S, Bertaso F, Eulenburg V, Lerner-Natoli M, Herin GA, Bauer L, Bockaert J, Fagni L, Betz H, Scheschonka A. 2008. Knock-In Mice Lacking the PDZ-Ligand Motif of mGluR7a Show Impaired PKC-Dependent Autoinhibition of Glutamate Release, Spatial Working Memory Deficits, and Increased Susceptibility to Pentylenetetrazol. *J Neurosci* **28**:8604–8614. doi:10.1523/JNEUROSCI.0628-08.2008